Tectonophysics 618 (2014) 79–101

Contents lists available at ScienceDirect

Tectonophysics

journal homepage: www.elsevier.com/locate/tecto

Fault damage zones of the M7.1 Darfield and M6.3 Christchurch earthquakes characterized by fault-zone trapped waves

Yong-Gang Li [a,*], Gregory P. De Pascale [b], Mark C. Quigley [b], Darren M. Gravley [b]

[a] Department of Earth Sciences, University of Southern California, Los Angeles, CA, USA
[b] Department of Geological Sciences, University of Canterbury, Christchurch, New Zealand

ARTICLE INFO

Article history:
Received 20 May 2013
Received in revised form 20 January 2014
Accepted 26 January 2014
Available online 2 February 2014

Keywords:
New Zealand
Christchurch earthquake
Darfield earthquake
Multiple ruptures
Fault rock co-seismic damage
Fault-zone trapped waves

ABSTRACT

To characterize the subsurface structure of the damage zones caused by the 2010–2011 Canterbury earthquake sequence in New Zealand's South Island, we installed two short linear seismic arrays; Array 1 across the Greendale Fault (GF) surface rupture and Array 2 over the surface projection of the blind Port Hills Fault (PHF) that ruptured in the 2010 M7.1 Darfield and 2011 M6.3 Christchurch earthquakes, respectively. We recorded 853 aftershocks for ~4 months after the Christchurch earthquake. Fault-zone trapped waves (FZTWs) identified at Array 1 for aftershocks occurring on both the GF and the PHF show that the post-S durations of these FZTWs increase as focal depths and epicentral distances from the array increase, suggesting an effective low-velocity waveguide formed by severely damaged rocks existing along the GF and PHF at seismogenic depths. Locations of aftershocks generating prominent FZTWs delineates the subsurface GF rupture extending eastward as bifurcating blind fault segments an additional ~5–8 km beyond the mapped ~30-km surface rupture into a zone with comparably lower seismic moment release west of the PHF rupture which extends westward to within 5.3 ± 1 km of the subsurface GF. The propagation of FZTW through the intervening 'gap' indicates moderate GF–PHF structural connectivity. We interpret this zone as a fracture mesh reflecting the interplay between basement faults and stress-aligned microcracks that enable the propagation of PHF-sourced FZTWs into the GF damage zone. Simulations of observed FZTWs suggest that the GF rupture zone is ~200–250-m wide, consistent with the surface deformation width. Velocities within the zone are reduced by 35–55% with the maximum reduction in the ~100-m-wide damage core zone corresponding with surface and shallow subsurface evidence for discrete fracturing. The damage zone extends down to depths of ~8 km or deeper, consistent with hypocentral locations and geodetically-derived fault models.

1. Introduction

Major crustal faults are typically composed of complex sets of slip planes, which are influenced by the presence of fault gouge and fluid and exhibit deformation that ranges from steady to stick slip (Scholz, 1990; Sibson, 2000). Many observations suggest that fault zone complexity may segment faults (Aki, 1984; Beck and Christensen, 1991; Li et al., 2002, 2003; Malin et al., 1989) or control the spatial and temporal variations of moment release in earthquakes (e.g. Harris and Day, 1993; Oglesby et al., 2003; Wald and Heaton, 1994). Geometrical, structural, and rheological fault discontinuities caused by spatial and temporal variations in strength and stress will also affect the earthquake rupture (e.g., Blanpied et al., 1992; Das and Aki, 1997; Ellsworth, 1990; Rice, 1992; Vidale et al., 1994). Rupture segments are often related to fault bends, step-overs, branches, and terminations that have been recognized by surface mapping (e.g., Johnson et al., 1994; Sieh et al., 1993), exhumation of fault rocks (e.g., Chester et al., 1993), or by seismic profiling and tomography (e.g., Thurber et al., 2004, 2006; Michelini and McEvilly, 1991; Michael and Eberhart-Phillips, 1991).

Intense fracturing during earthquakes, brecciation, liquid-saturation and possibly high pore-fluid pressure near faults have been thought to create low-velocity zones with widths ranging from a few hundred meters to a few kilometers (Mooney and Ginzburg, 1986). These naturally formed low-velocity zones can efficiently trap seismic waves generated by earthquakes occurring within or close to them and are thus called fault-zone trapped waves (FZTWs). Since FZTWs arise from coherent multiple reflections and corresponding high reflection coefficients at the boundaries between the low-velocity fault zone and the high-velocity surrounding rock, these waves are characterized by large amplitudes and dispersive wavetrains (Ben-Zion, 1998; Li and Leary, 1990; Li and Vidale, 1996; Li et al., 1990). Therefore, FZTWs can be used to resolve the high-resolution intra-fault structures and continuity of rupture zones as well as their temporal variations at seismogenic depths. The size and magnitude of the low-velocity anomalies on active faults as well as their variations in seismic velocity over the earthquake cycle have been observed in previous studies at the San Andreas fault at Parkfield, and rupture zones of the 1992 M7.4 Landers–1999 M7.1 Hector Mine, California earthquakes (Ellsworth and Malin, 2011;

* Corresponding author at: Department of Earth Science, University of Southern California, Los Angeles, California, 90089-0740, USA. Tel.: +1 213 740 3556; fax: +1 213 740 8801.
E-mail address: ygli@usc.edu (Y.-G. Li).

0040-1951/$ – see front matter © 2014 Elsevier B.V. All rights reserved.
http://dx.doi.org/10.1016/j.tecto.2014.01.029

Korneev et al., 2003; Li and Malin, 2008; Li and Vidale, 2001; Li et al., 1998, 2003, 2004, 2012a, b; Vidale and Li, 2003; Wu et al., 2010).

The 2010–2011 Canterbury earthquake sequence (CES) in New Zealand's South Island includes the 4 September 2010 Mw7.1 Darfield earthquake and three subsequent earthquakes greater than M_L6.0 (Fig. 1a), most notably the 22 February 2011 Mw 6.2 (M_L6.3) Christchurch earthquake that caused 185 fatalities, along with extensive liquefaction and co-seismic rock fall. All of these earthquakes occurred on previously unknown faults. The initiating 4 September 2010 Mw7.1 Darfield earthquake was a complex event, beginning at ca. 10.7 km depth on a steep reverse fault (Gledhill et al., 2011) and involving the rupture of 7–8 fault segments including E–W striking right-lateral faults, NE-striking reverse faults, NNW-striking left-lateral faults, and NW-striking normal right-lateral faults (Fig. 1a) (Beavan et al., 2012; Elliott et al., 2012). The largest moment release, as indicated from the GeoNet Regional CMT focal mechanism solution (http://www.geonet.org.nz/resources/earthquake/), and teleseismic analyses (USGS, http://earthquake.usgs.gov; Global CMT, http://www.globalcmt.org/) is consistent with the right-lateral rupture of the Greendale Fault (GF; equivalent to a Mw6.9–7.0 earthquake). Rupture of the GF produced a 29.5 ± 0.5 km long surface rupture (Barrell et al., 2011; Quigley et al., 2010, 2012) across a low relief Late Pleistocene alluvial plain (Forsyth et al., 2008). Maximum dextral displacements exceeded 5.2 m and maximum vertical displacements exceeded 1.5 m, and average net displacements along the fault length were 2.5 m. GF surface deformation was typically characterized by a ~50–150 m wide zone of distributed folding (Van Dissen et al., 2011) with an internal zone of discrete surface fracturing that ranges in width from 5 to 50 m (Fig. 1b). Major surface fractures with ≥ 30–50 cm slip were traced into the subsurface using offset sedimentary horizons and clast imbrications in the faulted gravels (Fig. 1c). Maximum subsurface slip was concentrated at depths of 2–6 km (Beavan et al., 2012) and may have exceeded 7 m over a strike length of ~7–8 km (Elliott et al., 2012). The combined subsurface GF length is inferred to be ~48 km (Beavan et al., 2012). The inferred rupture extents of other blind faults (Fig. 1) that ruptured in the Darfield earthquake range from 0.5–1 km depth (Beavan et al., 2012), suggesting that rupture likely ceased near the base of the Pliocene (~1 km) or Quaternary (~0.5 km) sedimentary deposits (Jogens et al., 2012). The Pliocene sequence is variably underlain by a 1–2 km thick package of Late Cretaceous to Neogene sedimentary and volcanic rocks and Mesozoic greywacke bedrock at seismogenic depths where major Canterbury earthquake sequence events initiated. Preliminary investigations of the GF suggest recurrence intervals of surface rupturing earthquakes on the order of 15–20 kyrs or longer, suggesting long time intervals over which interseismic fault annealing can occur. The GF is interpreted to be an inherited Cretaceous fault, based on parallelism with other known Cretaceous rift faults both onshore and offshore (Davy et al., 2012), and has become active in the modern tectonic regime due to progressive translation towards the rapidly deforming part of the Pacific–Australian plate boundary in New Zealand.

Following the 2010 M7.1 Darfield earthquake, aftershock activity was particularly concentrated at the eastern end of the GF in a 10 × 10 km area (Fig. 1). Earthquake focal mechanisms in this area indicate a complex regime predominated by sinistral 'tear faulting' on ~NNW-striking sub-vertical faults and dextral strike slip on E–W striking faults, with minor normal faulting on ~NW–SE striking faults and reverse-oblique faulting on ~NE–SW striking faults (Fig. 1a; Bannister and Gledhill, 2012; Sibson et al., 2011). Approximately 6 months after the Darfield earthquake, the 22 February 2011 Mw6.2 (M_L6.3) Christchurch earthquake occurred, with an epicenter approximately 40 km east of the Darfield earthquake epicenter (Fig. 1a). The Christchurch earthquake involved the rupture of 2–3 blind faults, henceforth referred to as the Port Hills Fault (PHF) system with reverse and right-lateral displacements (Fig. 1a; Beavan et al., 2012). The inferred tops of other blind faults were ~ 0.5 km depth below the surface, suggesting rupture termination in Miocene volcanic rocks. Maximum co-seismic slip was 2.5–3.0 m at depths of 4–6 km (Beavan et al., 2012; Elliott et al., 2012). The 13 June 2011 Mw6.0 (M_L6.4) earthquake likely involved an intersecting ENE-striking reverse-right lateral fault and NW-striking left-lateral fault with the deep rupture extending upward to ~1 km depth below the surface and maximum subsurface slip of < 1 m (Beavan et al., 2012).

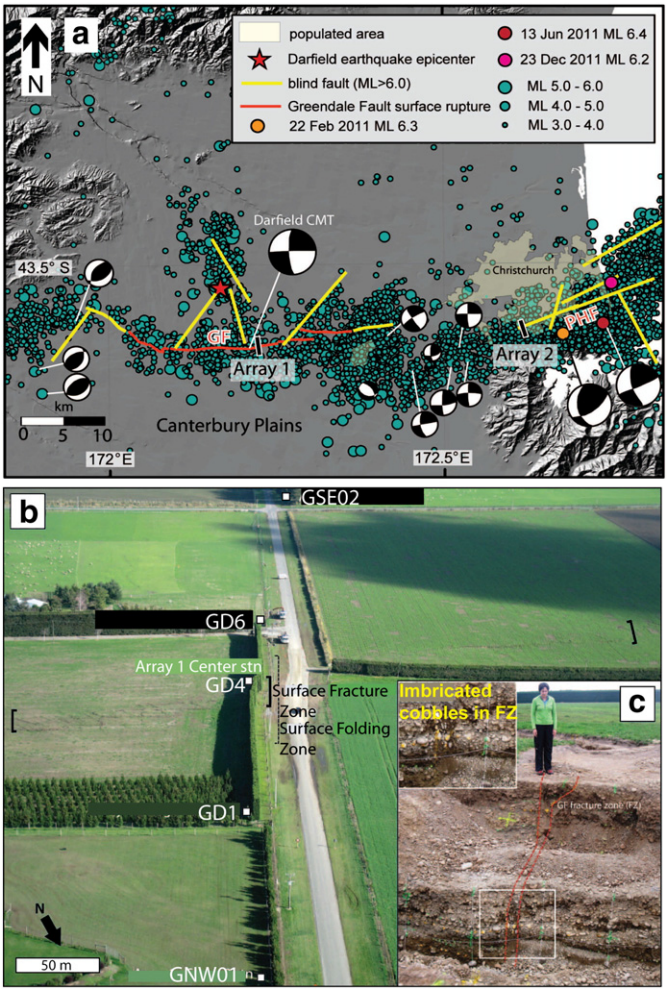

Fig. 1. (a) Epicenter locations for ML ≥ 3.0 events from 4 September 2010 to 10 February 2013 (data from www.geonet.org.nz). Projected surface locations of major faults in yellow (Beavan et al., 2012; Elliott et al., 2012) and location of mapped surface ruptures in red (Quigley et al., 2010, 2012). GF — Greendale Fault. PHF — Port Hills Fault. The NNW-striking fault north of the GF is a sinistral fault proposed by fault-zone trapped waves, consistent with Segment 6 in the slip model of Elliott et al. (2012). Locations of Arrays 1 and 2 are as shown. Focal mechanism solutions for selected earthquakes as shown are from Sibson et al. (2011) and Bannister and Gledhill (2012). We use the GeoNet Regional Centroid Moment Tensor solution for the Darfield earthquake (Darfield CMT) (http://www.geonet.org.nz/resources/earthquake/). Focal mechanisms indicate a variety of faulting, generally characterized by dextral strike–slip on E–W oriented faults (e.g., Darfield earthquake), sinistral strike–slip on NNW-oriented faults (e.g., 13 June earthquake), reverse slip on NE–SW oriented faults (area west of GF), normal slip on NW–SE oriented faults, and dextral-reverse slip on ENE-oriented faults (e.g., 22 Feb Christchurch earthquake). Focal mechanisms indicate that all of these fault types are present in the structurally complex area between the GF and PHF, although strike–slip faulting is most prevalent. (b) Aerial photograph of the GF surface rupture taken from a helicopter on 13 September 2010 after the 4 September 2010 Darfield earthquake. View is towards the south. Location of surface rupture is delineated by the 'surface fracturing zone', which consists primarily of en-echelon NW–SE and WNW–ESE trending Riedel fractures and E–W trending Y fractures, and a broader zone of distributed deformation referred to as the 'surface folding zone' (Quigley et al., 2012). Locations of Array 1 center station (GD4) and Stage 1 end points (GD1 and GD6) as shown, Stage 2 (extended array) end points are outside of the view of the photograph while stations GNW01 and GSE02 of the extended array are shown. (c) Photograph of excavation into the Greendale Fault 'surface fracturing zone' and within 10 m of the Array 1 center station. View is towards the east. Discrete fracture zone indicated by presence of surface fissures can be traced into the bottom of the excavation at > 3 m depth. Near bottom of trench, tectonically imbricated cobbles in the fault zone (inset) result from fault slip and resultant cobble rotation. Similar cobble rotations are likely to occur throughout the GF fracture zone.

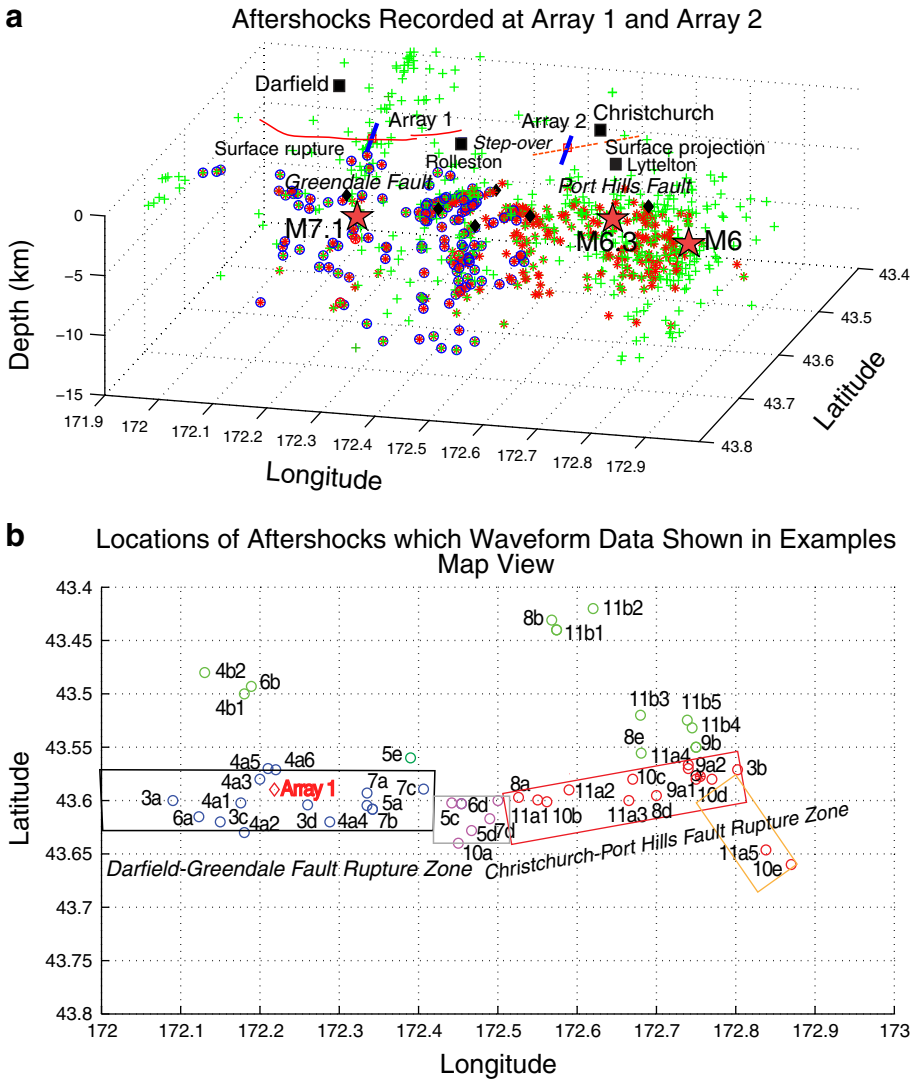

Fig. 2. (a) Hypocentral Locations of 853 aftershocks recorded at Array 1 and Array 2 (marked by blue bars) across the GF surface rupture (red line) and the surface projection (dashed brown line) of the blind PHF rupture are shown in a 3-D volume beneath Canterbury Plains. Red asterisks with blue circles denote aftershocks occurring within the GF surface rupture. Red asterisks without circles denote the PHF rupture segment. Prominent FZTWs were generated by these aftershocks and recorded at Array 1. Green pluses denote aftershocks for which no significant FZTWs were recorded at our two arrays. Stars denote the 2010 M7.1 Darfield mainshock, the 2011 M6.3 Christchurch earthquake and the 13 June 2011 M6 (M_L6.4) aftershock. Six black diamonds denote $M \geq 5$ aftershocks recorded at our arrays. Black squares denote cities and towns in the study area. (b) Map view of epicenters of the aftershocks recorded at Array 1 (marked red diamond), for which waveforms are shown in this article. Blue and red circles denote aftershocks occurring within GF rupture zone (marked by a blue band) and PHF rupture zone (marked by a red band), respectively, that generate significant FZTWs recorded at Array 1. Purple circles denote aftershocks occurring in the fault step-over zone. Green circles denote aftershocks without significant FZTWs. These aftershocks are numbered in order of waveform examples shown in Figs. 3 to 11 (Table 1).

The Christchurch earthquake and other earthquakes following the Darfield earthquake are forthwith referred to as aftershocks based on statistical merit (Shcherbakov et al., 2012). The close temporal coincidence of these major earthquakes on faults that either intersect (PHF and June earthquake source) or are separated by distances of ≤10–15 km (GF and PHF) raises important questions about fault damage zone characteristics, fault geometries, and crustal structure in the intervening areas. In this paper we use FZTWs to characterize the subsurface GF fault damage zone, image the blind segment of a PHF rupture zone and investigate crustal structure between these major faults (i.e. the seismic gap), in order to evaluate GF–PHF 'connectivity' with relevance for understanding fault evolution and earthquake potential in this area.

2. Data and waveform analyses

We installed two 250-m-long seismic arrays, each array consisting of 6 three-component seismometers with 50-m station spacing, to record FZTWs generated by aftershocks in the Canterbury region for ~4 months starting from 5 May 2011 (Fig. 1a). Array 1 was installed as a straight line of PASSCAL REFTEK130 instruments perpendicularly across the surface rupture on the central GF on the northern side of Highfield Road (hereafter the GF site) where the right-lateral slip of 4.5 m and vertical slip of 1.6 m along the GF were measured after the 2010 Darfield earthquake (Fig. 1b and c) (Barrell et al., 2011; Quigley et al., 2012). The center station of Array 1 was located at latitude of S43°35.649′, and longitude of E172°13.141′. The length of Array 1 encompassed both the zone of surface fracturing and a broader zone of distributed folding associated with GF displacement (Fig. 1b). Array 2 was installed near the suburb Cashmere in Christchurch (henceforth PHF site) and located at the approximate surface projection of the aftershock zone along the blind PHF which ruptured in the 2011 Christchurch earthquake but did not create a surface rupture (Bannister et al., 2011; Kaiser et al., 2012). The center station of Array 2 was located at latitude of S43°34.887′, and longitude of E172°35.720′. In the later

stage of our experiment starting from August 23, we removed 6 stations from Array 2 and added them into Array 1 at the GF site (Fig. 1b) to extend the full length of Array 1 to 950 m. The data recorded at Array 1 with the longer array length help us to better determine the width of low-velocity rupture zone on the GF site and distinguish FZTWs from surface waves. At each station, a PASSCAL REFTEK130 recorder with GPS powered by a deep-cycle battery charged with solar panel and a L22 2-Hz sensor was installed. The three-components of the sensor are vertical, parallel and perpendicular to the fault line. The seismometers recorded in continuous mode at 100 samples per second and were synchronized by internal GPS clocks. We recorded approximately 850 aftershocks during ~4 months at two arrays in our experiment, including the June 13th M_W6 ($M_L6.4$) aftershock and six $M \geq 5$ aftershocks (see Fig. 2a).

Since rocks along the GF and the PHF rupture zones experienced severe damage and meter-scale displacements during rupture in the Darfield and Christchurch earthquakes, the fault zone forms an effective low-velocity waveguide to trap seismic waves. We examined waveform data recorded at Array 1 and Array 2 for 853 aftershocks and identified FZTWs for study of subsurface damage structure associated with the 2010–2011 Canterbury earthquake sequence. The data recorded at Array 1 in general show good signal-to-noise ratio (>5) because the site is located on a quiet rural road with minimal traffic. Fig. 2a exhibits hypocenters of these 853 aftershocks occurring at different depths and epicentral distances from our seismic arrays under the Canterbury Plains. Locations of these aftershocks come from the earthquake catalog of New Zealand GEONET. Fig. 2b shows locations of the aftershocks for which waveforms are shown in examples in this article.

Fig. 3a and b show seismograms recorded at the 950-m-long extended-length Array 1 for two aftershocks occurring at 7–8-km depths on the GF and PHF, respectively, with epicentral distances of ~10-km west and ~45-km east of the array site. Locations of these aftershocks are shown in Fig. 2b and Table 1. We observed large-amplitude and long-duration wavetrains immediately after S-arrivals at stations in a range of ~200-m across the GF surface trace while shorter wavetrains were registered at stations farther away from this range. We measured post-S durations of FZTWs to be ~3.3-s and ~8-s, in which amplitudes of FZTWs at stations GD3, GD4, and GD5 located within the surface fracturing and folding zone (Fig. 1b) are above twice the level of the background noise coda, for these two aftershocks. Spectral amplitudes of seismograms consistently show ~3.3-s and ~8-s post-S durations of FZTWs at station GD3 within the Darfield/GF fracturing zone, but much shorter post-S durations (~1.5-s and ~3.0-s) of post-S wavetrains at station GNW02 450-m away from the GF surface trace for two aftershocks. We interpret the post-S wavetrains characterized by large amplitudes and long durations immediately following S-arrivals at near-fault stations in a range of ~250-m across the GF to be FZTWs trapped within the low-velocity rupture zone because they are observed for aftershocks and stations both located within or close to the fault zone. If these long wavetrains are surface waves propagating in the top layer, they should appear at all stations of Array, but not only at stations within the rupture zone.

In our study, we identify significant FZTWs generating by aftershocks within and close to the rupture zone based on a criteria: the ratio of post-S duration time of FZTWs to the P-to-S time measured at near-fault stations larger than 1.2. We set this ratio to satisfy a good condition of FZTW excitation and propagation within the low-velocity rupture zone. When this ratio is less than 1.2, we interpret that no significant FZTWs were generated and recorded at Array 1 for the aftershocks due to their locations away from the rupture zone or other reasons. The measured ratios for the two aftershocks in Fig. 3a and b are 1.7 and 1.3 (refer to Table 1). We observe that FZTWs sourced from a more distal aftershock (Fig. 3b) show longer wavetrains than those from the more proximal aftershock (Fig. 3a), although the relationship between the wavetrain length of FZTWs and their travel-distance is not linear. These observations suggest the existence of an effective low-velocity waveguide along the GF and PHF between Array 1 on the GF and the distal aftershock on the PHF, but the waveguide trapping efficiency may vary along multiple rupture segments and with depth.

In order to systematically document the subsurface damage zones along the multiple faults that ruptured in the 2010–2011 Canterbury earthquake sequence, we first examined aftershocks occurring around the GF, and then around the PHF.

2.1. The FZTWs recorded for aftershocks along Darfield/Greendale rupture zone

In this section, we illustrate the data recorded at Array 1 across the central GF and results from waveform analyses for aftershocks occurring on and off the GF at different depths and epicentral distances. Fig. 3c and d exhibit seismograms at 6 stations of Array 1, waveform amplitude envelopes, normalized spectral energy and band-pass filtered waveforms for two M2.2–2.5 aftershocks occurring at depths of 5-km and 9-km, respectively, within the Darfield/GF rupture zone with epicentral distances less than 4 km from the array site. The ray-paths between the array and aftershocks are sub-vertical. Waveform amplitude envelopes and spectra are computed using standard programs in Seismic Analysis Code (SAC). We measured durations of post-S wavetrain using a specific moving window (1-s width with 0.1-s step) starting from S-arrivals, in which amplitudes are above twice the level of the background noise coda in the same window length starting at 3 times of the P-to-S time from the S-arrival, resulting in ~1.8-s for the shallow aftershock at 5-km depth and ~3.5-s for the deep aftershock at 9-km depth. The ratios of post-S duration time to the P-to-S time for two aftershocks are 1.8 and 2.5, respectively (see Table 1). Spectral amplitudes of seismograms recorded at station GD3 show dominant energy at 3–7 Hz in1.8-s and 3.5-s time durations after S-arrivals for these two on-fault aftershocks, consistent with the post-S wavetrain lengths measured by moving window method. We interpret the post-S wavetrains with relatively large amplitudes and long durations immediately following S-arrivals

Fig. 3. Parallel-component seismograms recorded at 9 stations of expanded Array 1 to 950-m for (a) a M2.5 aftershock occurring on the GF ~10 km west of Array 1 site, and (b) a M5 aftershock occurring on the easternmost portion of blind PHF ~45 km east of GF site. Latitudes, longitudes and focal depths of the aftershocks as well as distances of stations from the surface trace of Greendale fault are shown in plot. Seismograms have been <8 Hz filtered and are with a fixed amplitude scale in each cross-fault profile, showing FZTWs with relatively large amplitudes and long post-S wavetrains at stations GD3, GD4, GD5, GD6 in the central portion (marked by a pair of vertical lines) of Array 1 across the GF. FZTWs generated by more distal on-fault aftershocks show much longer wavetrains (~8-s post-S duration) than those (~3.3-s post-S duration) generated by the nearer on-fault aftershock. Spectral amplitudes of vertical-component seismograms at station GD3 are computed and normalized with the color code of cool to hot ranging from 0 to 1, showing dominant FZTWs at 3–7 Hz in 3.3-s and 8-s time durations (marked by red bars at bottom) for the near aftershock on the GF in (a) and the distant aftershock on the PHF in (b), respectively. In contrast, spectral amplitudes show 1.5-s and 3.0-s time durations at the farther station GNW02 for these two on-fault aftershocks. (c) Vertical-component seismograms, amplitude envelopes, normalized spectral energy, and band-pass filtered waveforms at 6 stations of the original Array 1 for a M2.5 aftershock and (d) for a M2.2 aftershock occurring within the GF rupture zone near Array 1 site at 5-km and 9-km depths, respectively. The post-S durations of seismograms with large amplitudes and long wavetrains (marked by a pair of vertical lines) at 3 central stations GD3, GD4 and GD5 located within the damage core zone that corresponds with the zone of surface fracturing and folding identified in field investigations (Fig. 1b), are measured to be ~1.8-s and ~3.5-s on average at 3 stations with the standard deviations of ±0.2 s and ±0.3 s, for the shallow and deep aftershocks, respectively. For example, spectral amplitudes of vertical-component seismograms at station GD3 showing dominant FZTWs at frequencies 3–7 Hz in 1.8-s and 3.5-s time durations, consistent with the measurements by waveform moving window. Seismograms at station GD3 are also used for band-pass filtering in 5 frequency bands. The peak of envelopes denotes the arrival of FZTWs with its group velocity at the specific frequency band, showing dispersion of FZTWs traveling faster at the lower frequency than at the higher frequency.

(similar to those recorded at central stations of Array 1 shown in Fig. 3a and b) most likely as being FZTWs generated by aftershocks occurring within the low-velocity waveguide formed by severely damaged rocks along the Darfield/GF rupture zone at seismological depths.

We then applied five narrow band-pass filters with 1 Hz band at central frequencies of 1.75, 2.5, 3.5, 4.5, 5.5 Hz for seismograms recorded at station GD3 deployed on the surface trace of the GF at Array 1 site. The amplitude envelope peak of band-pass filtered seismograms denotes the arrival of dominant FZTWs at the specific frequency band. The band-pass filtered seismograms show dispersion feature of FZTWs with the higher group velocity at lower frequency owing to the constructive interference conditions of seismic waves within the low-velocity waveguide. We derived group velocities of FZTWs from multiple band-pass filtered seismograms for aftershocks occurring within rupture zones and used them as constraints on waveguide velocities in our model for rupture zone structure of the 2010–2011 Canterbury earthquake sequence.

Fig. 4 shows seismograms recorded at Array 1 and waveform analyses for the data from 6 on-fault aftershocks occurring along the central GF site at depths between 7 km and 16.4 km, and 2 aftershocks

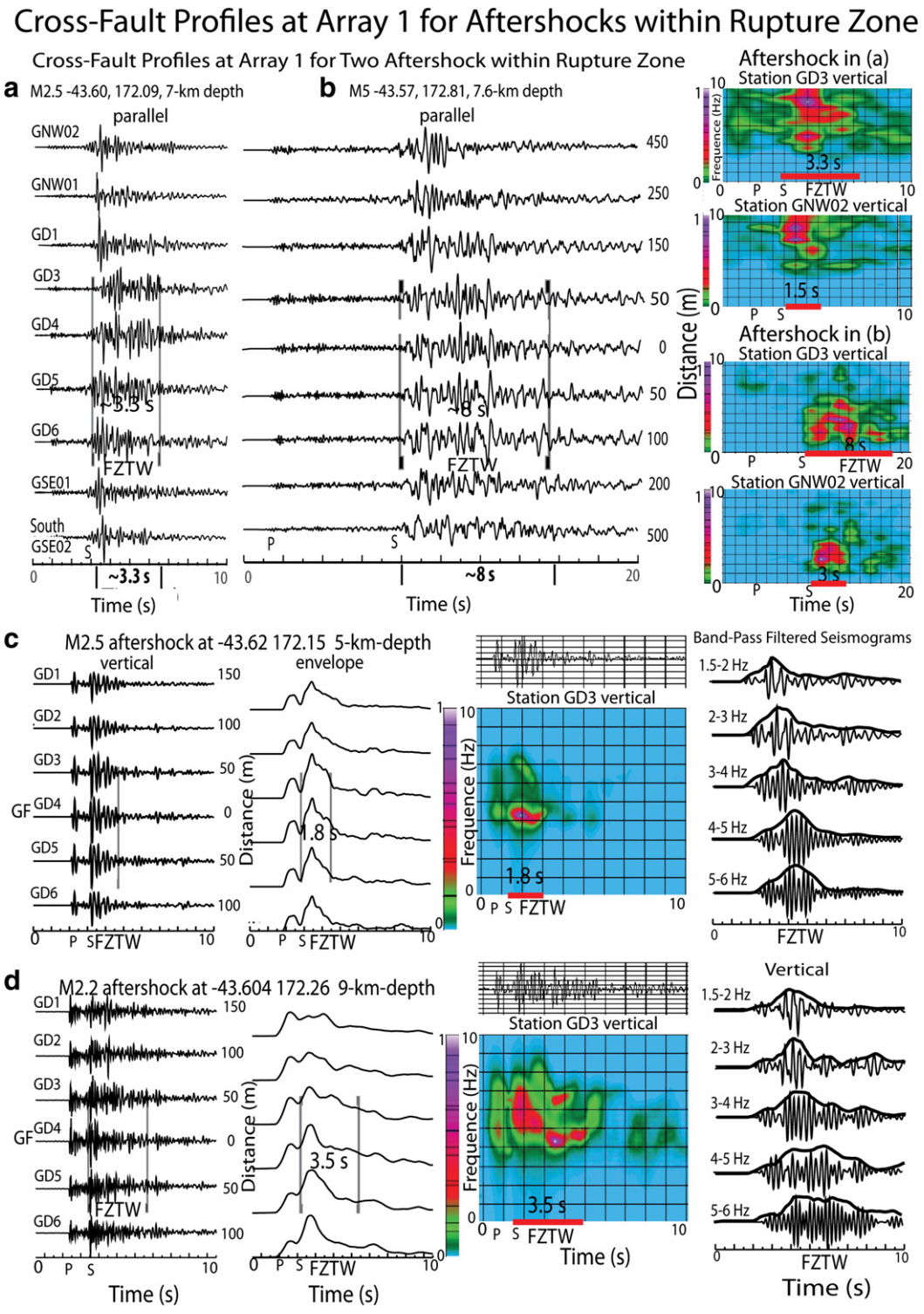

Table 1
Locations and Measurements of Aftershocks Numbered in Figures.

Label	Date 2011/m/d	Latitude	Longitude	Depth (km)	Mg	Post-S duration (second)	P-to-S Time (second)	Ratio	Figure
3a	09/01	−43.60	172.09	7.0	2.5	3.3	2.0	1.7	Fig. 3a
3b	09/01	−43.57	172.81	7.6	5.0	8.0	6.4	1.3	Fig. 3b
3c	05/05	−43.62	172.15	5.0	2.5	1.8	1.0	1.8	Fig. 3c
3d	05/22	−43.60	172.26	9.0	2.2	3.5	1.4	2.5	Fig. 3d
4a1	05/16	−43.60	172.18	8.5	3.4	2.8	1.3	2.2	Fig. 4a1
4a2	05/22	−43.63	172.18	8.6	2.5	2.8	1.3	2.2	Fig. 4a2
4a3	05/16	−43.58	172.20	7.0	2.7	3.0	1.4	2.1	Fig. 4a3
4a4	45/22	−43.62	172.29	7.8	2.3	3.3	1.7	2.0	Fig. 4a4
4a5	08/25	−43.57	172.22	10.5	2.5	3.8	2.3	1.7	Fig. 4a5
4a6	07/13	−43.57	172.21	16.4	2.6	5.0	2.1	2.4	Fig. 4a6
4b1	06/01	−43.50	172.18	6.7	2.6	1.6	2.0	0.8	Fig. 4b1
4b2	06/05	−43.48	172.13	10.0	3.0	1.3	1.4	0.5	Fig. 4b2
5a	08/30	−43.61	172.34	5.0	2.5	3.5	1.8	1.9	Fig. 5a
5b	08/31	−43.33	172.25	6.1	3.3	1.5	4.0	0.4	Fig. 5b
5c	08/30	−43.60	172.44	8.8	4.8	6.0	2.5	2.4	Fig. 5c
5d	08/28	−43.63	172.47	14.7	4.1	7.0	2.8	2.5	Fig. 5d
5e	08/28	−43.56	172.39	8.4	3.4	1.5	2.2	0.7	Fig. 5e
6a	09/01	−43.61	172.12	5.0	2.0	3.6	1.3	2.7	Fig. 6a
6b	09/01	−43.49	172.19	7.0	2.5	2.0	2.0	1.0	Fig. 6b
6d	08/30	−43.60	172.45	11.5	3.4	5.0	2.5	2.0	Fig. 6d
7a	09/01	−43.59	172.34	2.4	2.3	2.3	1.2	1.9	Fig. 7a
7b	08/31	−43.61	172.34	5.0	2.5	3.5	1.7	2.1	Fig. 7b
7c	08/31	−43.60	172.45	11.5	3.4	4.5	2.6	1.7	Fig. 7c
7d	08/31	−43.62	172.49	14.5	2.3	6.0	2.8	2.1	Fig. 7d
8a	06/21	−43.60	172.52	8.7	5.5	6.0	3.8	1.6	Fig. 8a
8b	05/09	−43.44	172.57	10.5	3.5	2.0	4.0	0.5	Fig. 8b
8d	05/19	−43.59	172.70	9.7	3.0	7.0	5.3	1.3	Fig. 8d
8e	08/30	−43.56	172.68	9.9	2.8	2.0	5.5	0.4	Fig. 8e
9a1	06/13	−43.58	172.75	8.9	6.0	8.0	6.0	1.3	Fig. 9a1
9a2	06/13	−43.57	172.74	6.4	4.4	8.0	6.0	1.3	Fig. 9a2
9b	05/19	−43.55	172.75	5.0	2.5	2.0	5.7	0.4	Fig. 9b
10a	08/30	−43.64	172.45	5.0	3.1	4.8	3.5	1.4	Fig. 10a
10b	08/29	−43.60	172.55	6.5	3.1	5.5	4.0	1.4	Fig. 10b
10c	08/29	−43.58	172.67	5.0	3.0	6.5	5.2	1.3	Fig. 10c
10d	09/01	−43.58	172.77	9.0	2.2	7.5	6.0	1.3	Fig. 10d
10e	06/15	−43.66	172.87	5.0	4.3	8.5	6.6	1.3	Fig. 10e
11a1	05/10	−43.60	172.50	5.0	3.0	6.0	3.8	1.6	Fig. 11a1
11a2	06/09	−43.59	172.59	5.0	2.6	6.5	4.0	1.4	Fig. 11a2
11a3	05/07	−43.60	172.67	5.2	4.0	6.7	5.0	1.4	Fig. 11a3
11a4	06/13	−43.56	172.74	6.4	4.4	8.0	5.5	1.5	Fig. 11a4
11a5	06/14	−43.64	172.84	5.9	5.0	8.5	6.8	1.3	Fig. 11a5
11b1	05/09	−43.44	172.57	10.5	3.5	1.5	4.8	0.3	Fig. 11b1
11b2	05/09	−43.42	172.62	5.0	2.8	2.0	5.0	0.4	Fig. 11b2
11b3	06/21	−43.52	172.68	12.0	3.3	3.0	5.2	0.6	Fig. 11b3
11b4	05/19	−43.55	172.75	5.0	2.5	2.0	5.2	0.4	Fig. 11b4
11b5	06/17	−43.53	172.75	5.3	4.4	3.0	5.8	0.5	Fig. 11b5

Note: Labels of aftershocks in Table 1 are shown in Fig. 2b.

occurring ~10-km away from the GF. The ray-paths between the array and these on-fault aftershocks have the incident angle smaller than 30° with respect to vertical. We measured 2.8-s to 5-s durations of post-S wavetrains at stations located in the surface fracturing and folding zone for six aftershocks, with longer wavetrains for deeper events. The ratios of post-S duration time of FZTWs to the P-to-S time for these aftershocks are measured to be 1.7–2.4 (see Table 1) larger than 1.2, showing a good excitation and transportation of FZTWs from the on-fault aftershocks. In contrast, much shorter (1.3–1.6 s) post-S wavetrains with the ratios <1.2 are registered for the aftershock ~10 km away from the rupture zone.

Observations of these FZTWs recorded at central stations of Array 1 for on-fault aftershocks, therefore, indicate a distinct low-velocity zone composed by severely damaged rocks along the central GF extending from the surface to downward to ~8–10 km depth or deeper, consistent with the hypocentral depths and geodetic fault models (e.g., Beavan et al., 2010, 2012; Elliott et al., 2012).

We interpret the long post-S wavetrains generated by on-fault aftershocks (Fig. 4a1 to a6) and recorded at near-fault stations of Array 1 most likely to be FZTWs rather than surface waves. If these waves are surface waves, they should be also generated by off-fault aftershocks (Fig. 4b1, b2) occurring at the similar depths and distances as the on-fault aftershocks and recorded at the same stations of Array 1. In Fig. 3a and b, we have showed that significant FZTWs recorded at near-fault stations in the ~200–250-m range across the GF but not at stations further away from the rupture zone. If the long wavetrains are surface waves, they should appear at all stations of Array 1 for aftershocks despite of their locations within or away from the low-velocity rupture zone. In the following examples, we shall further show that significant FZTWs were recorded for both aftershocks and stations located within or close to the rupture zone, but neither for aftershocks nor for stations away from the rupture zone.

Fig. 5a shows FZTWs with large amplitudes and 3.5-s post-S duration at central stations of length-extended Array 1 located within the ~200-m-wide rupture zone, but shorter (~1.5-s) wavetrains at 4 farther stations for a M2.5 aftershock occurring ~10 km east of the array within the central Darfield/GF rupture zone. In contrast, much shorter post-S wavetrains (~1.5-s) appear at all stations of Array 1 for an aftershock ~20 km north of the rupture zone (Fig. 5b). The ratios of post-S duration time of FZTWs to the P-to-S time are measured to be 1.9 at on-fault station GD3 and 0.8 at away-fault station GSW01 for the on-fault aftershock, but 0.4 at all stations for the off-fault aftershock (see Table 1).

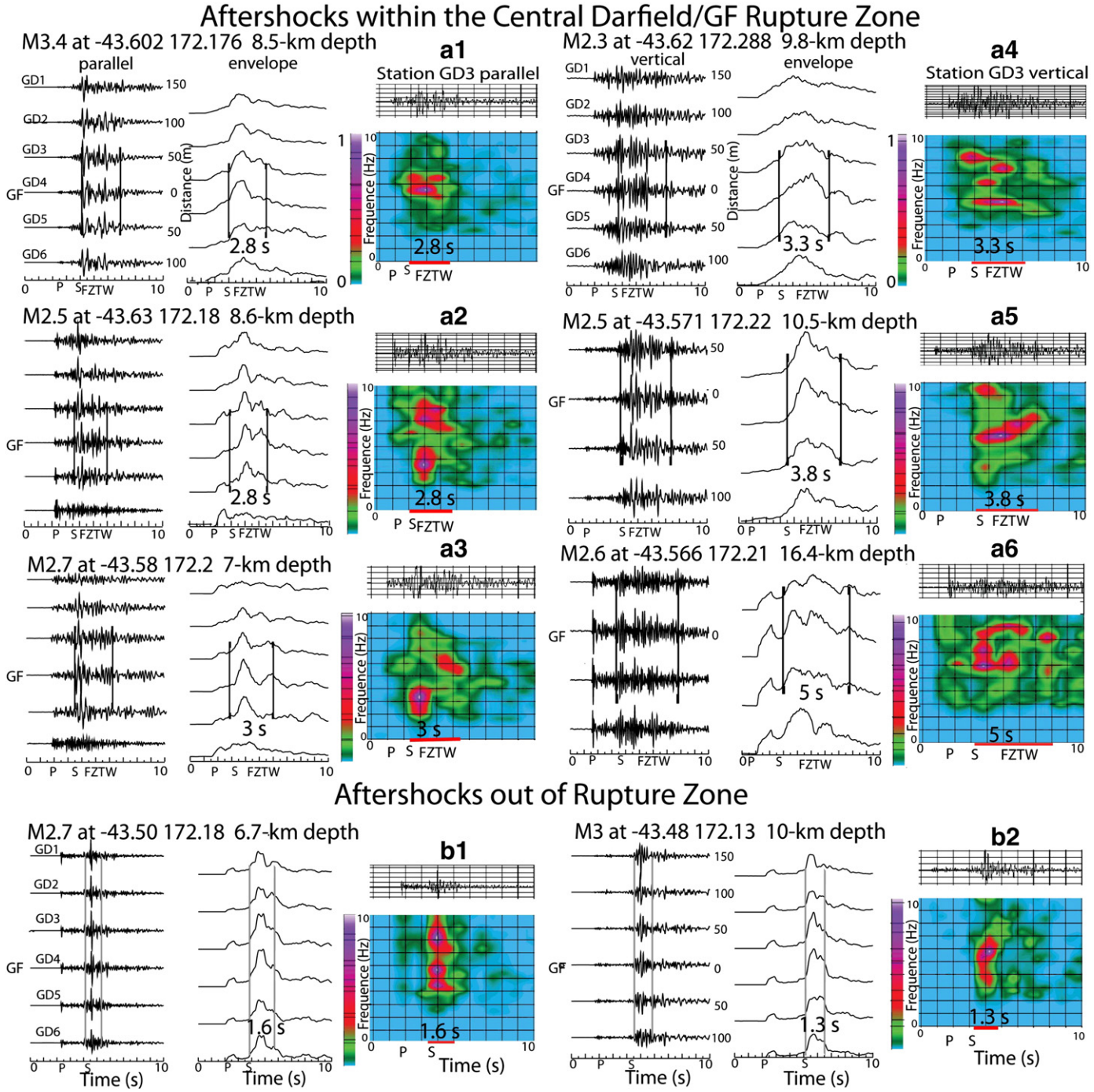

Fig. 4. left: Parallel-component seismograms, amplitude envelopes, and normalized spectral energy registered at 6 stations of the original Array 1 across the GF for (a1)–(a3) 3 aftershocks occurring within the central GF rupture zone at depths of 7–8.6 km and epicentral distances less than 3 km, and (b1) an off-fault aftershock at 10-km depth and ~8 km north of GF site. Locations and magnitudes of these events are shown in plot. Other notations are same as in Fig 3. The interpreted FZTWs with post-S durations of 2.8–3-s in average are registered at 3 central stations located within the rupture core zone for on-fault aftershocks while much briefer (1.6-s duration) S waves are dominant in seismograms at all stations for the far off-fault aftershock. For example, normalized spectral amplitudes of parallel-component seismograms at station GD3 show dominant FZTWs at frequencies 2–7 Hz in time windows marked by red bars at bottom. right: Same as in left, but for (a4)–(a6) 3 deep on-fault aftershocks and (b2) an off-fault aftershock at depths of ~10–16 km. Post-S durations of FZTWs for on-fault aftershocks increase from 3.3-s to 5-s as their focal depths increase from ~8 km ~16 km, while much shorter S waves (e.g. 1.3-s at station GD3) are registered for the aftershock ~10-km away from the rupture zone.

The results from waveform and spectral analyses of these data further suggest the long wavetrains following S-arrivals at near-fault stations of Array 1 to be FZTWs excited by the on-fault aftershock and propagating within the low-velocity waveguide formed by severe rocks along the Darfield/GF rupture zone. If they were surface waves, the long wavetrains should appear at all stations of Array 1 despite aftershock locations within or away from the rupture zone. The data recorded at the full-length Array 1 help us to distinguish FZTWs from surface waves and determine the width (~200-m) of the low-velocity waveguide formed by severely damaged rocks along the central GF rupture segment at Array 1 site.

We then exhibit the data at the full-length Array 1 for deep aftershocks occurring at 8.8–14.7 km depths and ~19–22 km east of the array site and ~5–8 km east of the GF surface rupture (Fig. 5c and d). FZTWs with 6–7-s post-S durations and ratio to the P-to-S time of 2.4–

2.5 (see Table 1) present at central stations of Array 1 for two aftershocks, indicating that the low-velocity waveguide formed by damaged rocks along the GF might extend eastward additional 5–8-km beyond the ~30-km-long surface rupture and to depths of at least ~8-km beneath the surficial fault step-over. We interpret that these deep aftershocks occurred on the eastward blind extension of the Darfield/GF surface rupture mapped by Quigley et al. (2010, 2012). In contrast, shorter (1.5-s) post-S wavetrains with the ratio to the P-to-S time of 1.1 (see Table 1) were registered at all stations of Array 1 for the aftershock occurring ~3-km away from the rupture zone (Fig. 5e).

Fig. 5e shows normalized spectral amplitudes of seismograms at stations of the full-length Array 1 for the on-fault aftershock in Fig. 5a show FZTWs with ~3.5-s duration at near-fault stations, but shorter post-S duration (1.5–1.8 s) at farther stations for the same event. In contrast, short post-S wavetrains (~1.5-s duration) were registered at near- and away-fault stations of Array 1 for the off-fault aftershock in Fig. 5e. Therefore, we interpret the long post-S wavetrains recorded at the central stations within Darfield/GF rupture zone for on-fault aftershocks as being FZTWs, but not surface waves, because these long wavetrains are recorded only for both aftershocks and stations located within or close to the low-velocity rupture zone. If these waves are surface waves, they should appear at all stations of Array 1 for aftershocks occurring either within or away from the rupture zone.

More examples of seismograms recorded at the full-length Array 1 are shown in Fig. 6. Fig. 6a, and b exhibit seismograms for a pair of aftershocks occurring within and away from GF rupture zone, at depths of 5–7-km and ~9-km west of Array 1. We observe post-wavetrains with large amplitudes and 3.5–3.7-s durations at central stations within the ~200-m wide surface fracturing and folding zone for the on-fault aftershock, but shorter post-S wavetrains (~2-s) at all stations of Array 1 for the aftershock ~10-km north of the GF (Fig. 6c). The ratio of post-S duration time to P-to-S arrival time measured at near-fault stations of Array 1 for the on- and off-fault aftershocks are 2.7 and 1.0, respectively (see Table 1). For another on-fault aftershock (in Fig. 6d) at 11.5-km depth and ~19-km east of Array 1, we observe post-S wavetrains with large amplitudes and ~5-s duration at central stations but shorter wavetrains at farther stations (e.g. ~2-s at station GWN02 450-m from the fault trace). The ratios of post-S duration time to P-to-S arrival time are 2.0 and 0.8 at the central and farther stations of Array 1, respectively, for this on-fault aftershock. These observations and results from waveform analyses support our interpretation that the long post-S wavetrains recorded at the central stations of Array 1 for on-fault aftershocks are FZTWs excited and propagating within a distinct low-velocity waveguide along the Darfield/GF rupture zone rather than surface waves. We observe the longer post-S wavetrains (~5-s) recorded at central stations for the on-fault aftershock at longer distance (in Fig. 6d) than those (~3.5-s) for the nearer aftershock (in Fig. 6a). Because significant FZTWs are observed for the aftershock (in Fig. 6d) occurring ~6-km beyond the east end of GF's surface rupture, we interpret that the Darfield/GF rupture zone extends eastward along the blind fault segment confined by aftershock lineaments at seismogenic depths (Bannister et al., 2011; Syracuse et al., 2013).

Fig. 7 illustrates that post-S durations of FZTWs increase as their travel distances along the rupture zone increase. FZTWs generated by 4 on-fault aftershocks occurring at depths of 2.4–14.5-km and epicentral distances of ~10–22-km east of Array 1 show post-S durations of FZTWs increasing from 2.3-s to ~6-s (denoted by the move-out of FZTW arrival times in the plot). Ratios of post-S duration time to the P-to-S time for these on-fault aftershocks are between 1.7 and 2.1 (see Table 1). Observations of FZTWs shown in this section illuminate a distinct low-velocity waveguide formed by severely damaged rocks during dynamic rupture in the 2010 Darfield earthquake, extending at least ~36-km along the central GF and its blind extension between longitudes of ~172.0° and 172.45°, and downward to the depth of ~8–10 km or deeper, consistent with hypocentral depths and geodetic fault models in published papers (Elliott et al., 2012; Beavan et al., 2010, 2012). We explain that the east 5–8-km extension of Darfield rupture zone beyond the 30-km-long GF's surface rupture runs along blind sinistral ~NNW-striking sub-vertical faults and dextral strike slip on E–W striking faults into the step-over between the GF and PHF where rocks might have experienced moderate damage due to induced slipping and/or strong shaking during the 2010 Darfield mainshock and large (M ≥ 5) aftershocks (Syracuse et al., 2013).

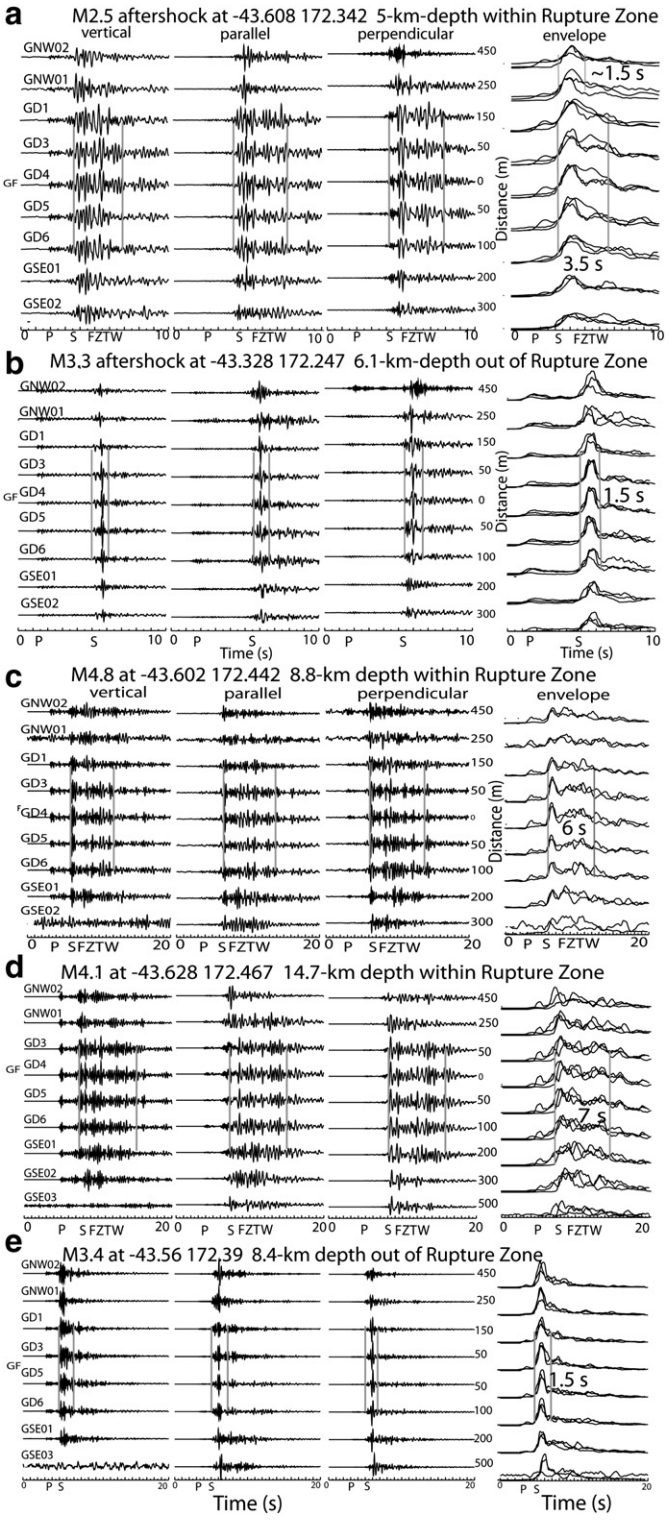

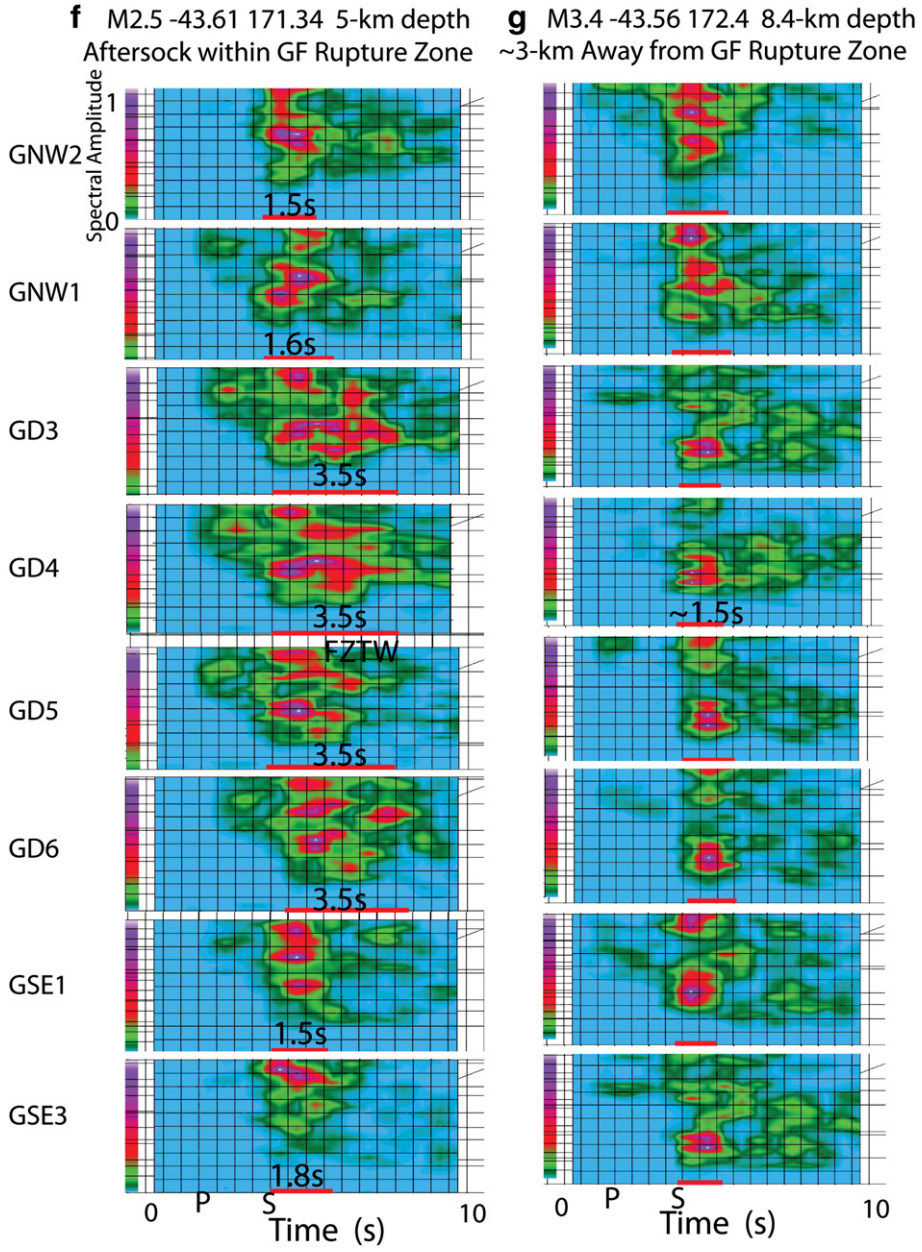

Fig. 5. (a) Three-component seismograms and amplitude envelopes recorded at the length-expanded Array 1 for a M2.5 aftershock occurring within GF rupture zone at 5 km depth and ~10 km east of GF site, showing relatively longer post-S wavetrains (interpreted as being FZTWs) at 5 central stations within the ~250-m-wide rupture zone (marked by a pair of vertical lines) than those at 4 farther stations GNW01, GNW02, GSE01 and GSE02. Amplitude envelopes of three-component seismograms are overlapped with a fixed scale in each plot. The measured durations of post-S wavetrains at central stations GD3 and GD4 are ~3.5 s, but ~1.5 s at farther station GNW01. (b) Same as in (a), but for a M3.3 aftershock occurring at 6.1-km depth, ~22 km north of the rupture zone. Much shorter (~1.5-s) S-waves are dominant at all stations of Array 1. (c) and (d) Same as in (a), but for M4.8 and M4.1 on-fault aftershocks occurring at 8.8-km and 14.7-km depths beneath the fault step-over, ~18–22-km east of Array 1. FZTWs with relative large amplitudes and long duration appear at stations within ~250-m wide rupture zone for these two aftershocks. We measured ~6-s and ~7-s post-S durations of FZTWs at stations GD3 and GD4 for them. (e) Same as in (b), but for a M3.4 aftershock occurring at 8.4-km depth, ~3 km north of the rupture zone. Much shorter (~1.5-s) post-S wavetrains appear at all stations of Array 1. (f) Normalized spectral amplitudes of vertical-component seismograms at stations of Array 1 for the on-fault aftershock in (a) show FZTWs with large amplitudes at frequencies 3–6 Hz and ~3.5-s duration at 4 near-fault stations, but shorter post-S duration (1.5–1.8 s) at 4 farther stations for the same event. (g) Same as in (f), but for the off-fault aftershock in (e), showing much shorter wavetrains (~1.5-s duration) at all stations of Array 1.

2.2. The FZTWs recorded for aftershocks along Christchurch/Port Hills rupture zone

In this section, we present data recorded at Array 1 across the GF surface rupture for aftershocks occurring on and off the blind Port Hills fault which ruptured in the 2011 M6.3 Christchurch earthquake. Fig. 8a exhibits seismograms and results of waveform analyses for a M5.5 event of clustered aftershocks occurring on the PHF at 8.7-km depth and ~25 km east of Array 1, at the west end of the delineated Christchurch aftershocks and approaching the dilatational step-over between the GF and the PHF (see Fig. 1). FZTWs excited by this on-fault aftershock show large-amplitude wavetrains with ~6-s post-S durations and the ratio to the P-to-S time of 1.6 (see Table 1) at central stations of Array 1. In contrast, much shorter post-S wavetrains (~2-s) with the ratio to the P-to-S time of 0.5 were registered at the same stations for the aftershock occurring at the similar dept of 10.5-km depth but ~12-km north of the on-fault aftershock (Fig. 8b). Fig. 8c exhibits normalized spectral energy of vertical-component seismograms at station GD3, showing 6-

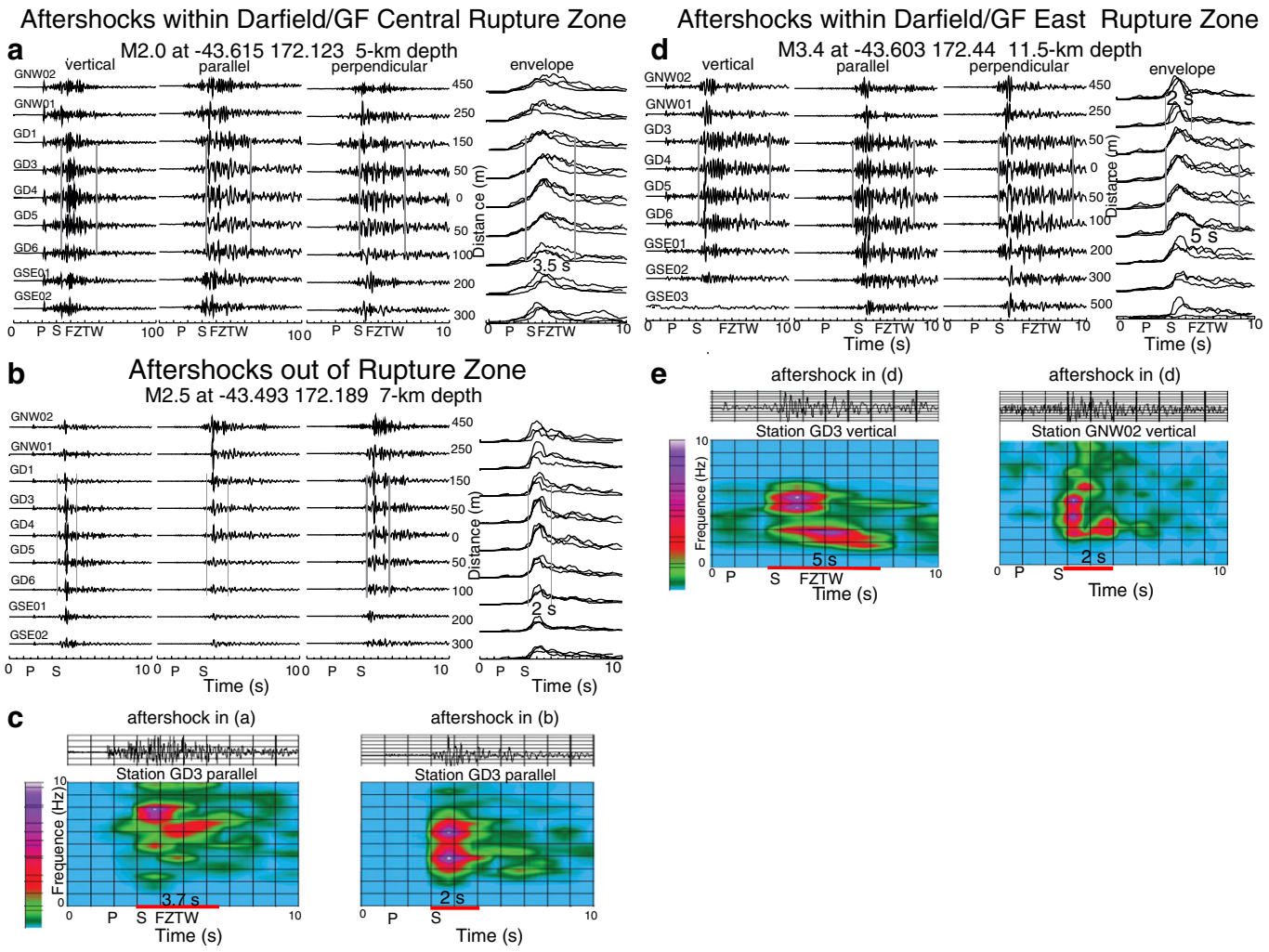

Fig. 6. (a) Three-component seismograms and amplitude envelopes recorded at the length-expanded Array 1 for a M2 aftershock occurring at 5-km depth within the central GF rupture zone, ~9 km west of the array. Large-amplitude long-duration post-S wavetrains appearing at stations in the central portion of Array 1 within the 250-m wide rupture zone (marked by a pair of vertical lines) are interpreted as FZTWs. The post-S durations of FZTWs at stations G3 and G4 are measured to be 3.5-s. (b) Same as in (a), but for a M2.5 off-fault aftershock occurring at 7-km depth, ~10 km north of the array. S waves with shorter wavetrains (2-s) are dominant in seismograms at all stations of Array 1. (c) Normalized spectral amplitudes of parallel-component seismograms at station GD3 show 3.7-s and 2-s durations of post-S wavetrains for the on- and off-fault aftershocks, respectively. (d) Same as in (a) but for a M3.4 aftershock occurring at 11.5-km depth within the easternmost portion of GF rupture zone, ~19 km east of the array. Seismograms show ~5-s post-S duration of FZTWs with large amplitudes at central stations of Array 1 in the 200–250-m wide rupture zone and shorter wavetrains (~2-s) at farther stations GNW01 and GNW02 located at 250-450-m north of the GF. (e) Normalized spectral amplitudes of vertical-component seismograms at stations GD3 and GNW02 for the aftershock in (d).

s and 2-s post-S durations for the on- and off-fault aftershocks in Fig. 8a and b, respectively. The entire duration of FZTWs generated by the on-fault aftershock likely includes a 4-s early duration.

In Fig. 8d and e, we show seismograms and their spectral energy at length-extended Array 1 across the central GF for a pair of M2.8–3 aftershocks occurring on the PHF and ~3-km north of the fault, respectively, at depths of 9.7–9.9 km and ~40 km east of the array. FZTWs with large amplitudes and ~7-s post-S duration measured at near-fault stations GD3–GD6 in the range of ~200-m, but shorter wavetrains (1.5–2.0 s) at farther stations for the on-fault event. In contrast, for the off-fault aftershock, much shorter post-S wavetrains (~1–2-s) appear at all stations of Array 1. The entire FZTW wavetrains likely consist of two successive phases (particularly seen in spectral energy plot) with an early phase in ~4-s duration for the aftershock occurring on the PHF in the east side of the step-over between the GF and the PHF. We tentatively interpret that there is a strong heterogeneity (rock damage magnitude and geometry) of the low-velocity waveguide beneath the surficial fault step-over, which might cause the multiple phases of FZTW wavetrains.

In our experiment, we recorded the June 13th M6 occurring on the east portion of Christchurch/PHF rupture zone, ~42 km east of Array 1. Fig. 9 exhibits seismograms and waveform analyses for this M6 and one of its clustered aftershocks (numbered by 9a1 and 9a2 in Fig. 2b and Table 1), showing ~8-s post-S durations of the entire FZTW wavetrains with ~4.5-s early phase (seen better in spectral energy plot). In contrast, shorter (2.5-s) post-S wavetrains are registered for the aftershock ~5-km north of the rupture zone. Ratios of the entire duration time of FZTWs to the P-to-S time are 1.4 for the on-fault aftershocks but 0.4 for the off-fault event. Examples shown in Figs. 8 and 9 illustrate that the post-S durations of entire FZTW wavetrains increase from ~6-s to ~8.5-s as hypocentral distances of on-fault aftershocks increase from ~27-km to ~43-km east of Array 1, but the early-phase remains in ~4-4.5 s.

The relationship between post-S durations of FZTWs and their travel distances along the rupture zone is apparent in Fig. 10. The wavetrains of FZTWs generated by five aftershocks occurring along Christchurch/PHF rupture segment increase from ~4.8-s to ~8.5-s as their travel distances increase from ~20-km to ~50-km (marked by the move-out of FZTW arrival times in the plot) while the duration of early-phase FZTWs remains ~4-s in the entire wavetrains. Ratios of the entire duration time of FZTWs to the P-to-S time for the on-fault aftershocks are 1.3–1.4. These observations suggest that an effective low-velocity

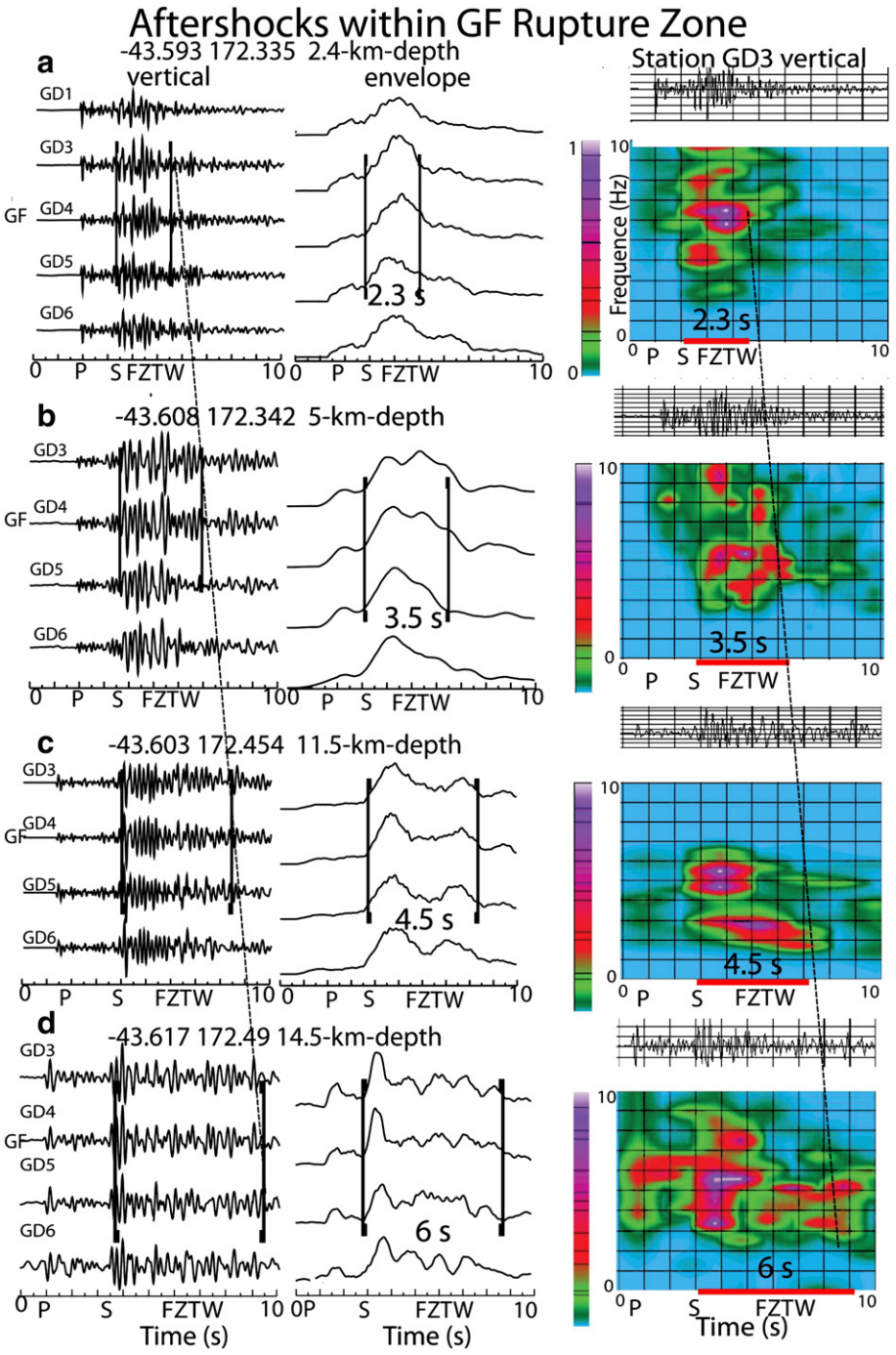

Fig. 7. Vertical-component seismograms, amplitude envelopes, and normalized spectral energy registered at 4 central stations of Array 1 for 4 aftershocks occurring within rupture zone east of the array. Post-S durations of these FZTWs increase from 2.3-s to ~6-s (in average of measurements at stations GD3, GD4 and GD5 within the damage core zone) as event focal depths increase from 2.4 km to 14.5 km and epicentral distances increase from ~10-km to ~22-km. Normalized energy of vertical-component seismograms at station GD3 shows 2.3-, 3.5-, 4.6- and 6-s durations of FZTWs for these aftershocks. The move-out of FZTW arrival times versus travel distances is denoted by a dashed line, illuminating a remarkable low-velocity waveguide along the Darfield/GF rupture zone likely across seismogenic depths.

waveguide extends eastward ~50-km from Array 1 along the Darfield/GF rupture segment through the fault step-over to the Christchurch/PHF rupture segment because PHF-sourced FZTWs propagated into the GF damage zone, but the waveguide might possess strong variations in the geometry (orientation from W–E to NW–SE) and velocities (smaller velocity reduction) beneath the surficial fault step-over between the two main rupture segments to distort wavetrains of FZTWs. These features are further shown in the following examples of seismograms and modeling of FZTWs.

Fig. 11 shows seismograms, amplitude envelopes, and spectral energy for 5 aftershocks occurring within the PHF rupture zone at different depths and epicentral distances, and 5 off-fault aftershocks occurring at similar depths and epicentral distances as those on-fault aftershocks. We observe that post-S durations of FZTWs generated by on-fault aftershocks increase from 6 s to 8.5 s as travel distances increase from ~25 km to ~50 km while early-phase FZTWs remain ~4-s. In contrast, brief wavetrains of S-waves with much shorter duration (~2–3-s) and flat changes are registered at 6 stations of Array 1 for the off-fault

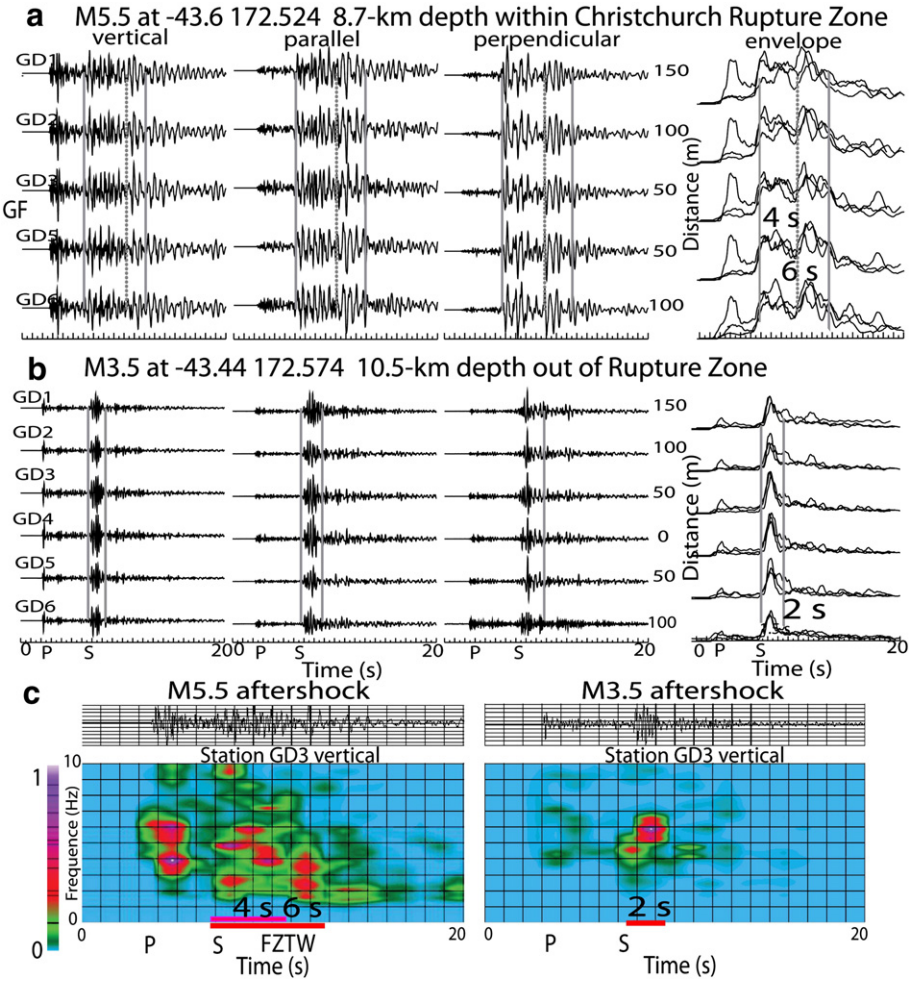

Fig. 8. (a) Three-component seismograms and amplitude envelopes at stations of the original Array 1 within the 250-m range across the central GF for a M5.5 aftershock occurring at depth of 8.7 km and ~25 km east of GF site, around the west end of the PHF. FZTWs with large amplitudes and ~6-s post-S duration averaged in three-component seismograms (marked by two vertical gray lines). These FZTWs likely show an early phase of ~4-s duration (marked by a vertical dot line in seismograms and amplitude envelopes). (b) Same as in (a) but for a M3.5 aftershock occurring at 10.5-km depth north of Christchurch City, ~12-km north of the PHF. Much shorter post-S wavetrains (~2-s) were registered for this off-fault event. (c) Normalized spectral energy of vertical-component seismograms at station GD3 show 6-s and 2-s post-S durations (marked by horizontal red bars) for the on- and off-fault aftershocks in (a) and (b), respectively. The entire duration of FZTWs generated by the on-fault aftershock includes a 4-s early duration (marked by a horizontal pink bar). (d) Parallel-fault component seismograms (top) and normalized spectral energy (bottom) at length-extended Array 1 across the central GF for a M3 aftershock occurring on the PHF at depth of 9.7 km and ~40 km east of the array. FZTWs with large amplitudes and ~7-s post-S duration measured at near-fault stations GD3–GD6, but shorter wavetrains (1.5–2.0 s) at farther stations. The FZTWs also likely show an early phase of ~4-s duration. (e) Same as in (d) but for a M2.8 aftershock occurring at 9.9-km depth north of ~3-km north of the PHF. Much shorter post-S wavetrains (~1–2-s) are registered at all stations of Array 1 for this off-fault event.

aftershocks. Ratios of the entire duration time of FZTWs to the P-to-S time are 1.3–1.6 for on-fault aftershocks but 0.3–0.6 for off-fault events (see Table 1).

We have measured post-S durations of FZTWs recorded at Array 1 for ~80 aftershocks occurring within or close to the GF rupture zone at different focal depths (~2–15 km) and epicenters between ~171.9° and 172.45° (~45-km along the fault line) versus their locations with respect to Array 1 site (see Fig. 12a). These aftershocks are selected based on the following criteria: the ratio of measured post-S duration time of FZTWs to the P-to-S time larger than 1.2 to assure good excitation and propagation of FZTWs (characterized by large amplitudes and long wavetrains after S-arrival) within the low-velocity waveguide along the Darfield/GF rupture zone. The measurements show that post-S durations of FZTWs increase from ~2-s to ~5-s as hypocentral distances of these aftershocks increase from ~8-km to ~23-km (Fig. 12b). We interpret that the distinct low-velocity waveguide along the GF is mainly formed by severely damaged rocks caused by the dynamic rupture in the 2010 M7.1 Darfield earthquake. The total length of the Darfield/GF rupture zone is ~45-km although only a 30-km-long portion is exposed at the ground surface. Our interpretation from FZTWs is consistent with the geodetic and InSAR image (Beavan et al., 2011; Elliott et al., 2012) and aftershock lineaments (Quigley et al., 2012; Syracuse et al., 2013). The InSAR line-of-sight displacement field indicates the main fault rupture in the 2010 Darfield event is approximately 45 km long, and is confined largely to the upper 10 km of the crust.

We also measured post-S durations of FZTWs recorded at Array 1 for ~150 aftershocks occurring within or close to the PHF rupture zone at different focal depths (~3–10 km) and epicenters between ~172.45° and ~172.82° versus event locations with respect to Array 1 (Fig. 12a). The aftershocks in the plot are selected based on the same criteria used for those GF-aftershocks. The measurements show that post-S durations of the entire FZTW wavetrains increase from ~5-s to ~9-s as hypocentral distances of these aftershocks increase from ~25-km to ~55-km (Fig. 12b). However, durations of the early-phase FZTWs remain ~3.5–4.5-s as travel distances of those aftershocks increase. We tentatively interpret that the low-velocity waveguide on the central PHF might extend westward along aftershock lineaments (Bannister et al., 2011; Syracuse et al., 2013) beneath the east portion of fault step-over zone (between longitudes ~172.45° and 172.55°) (see Fig. 1). This low-velocity waveguide might also extend further eastward (east of longitude 172.75°) to the rupture zone of the June 13th M6 aftershock on a blind conjugate fault (Fig. 1).

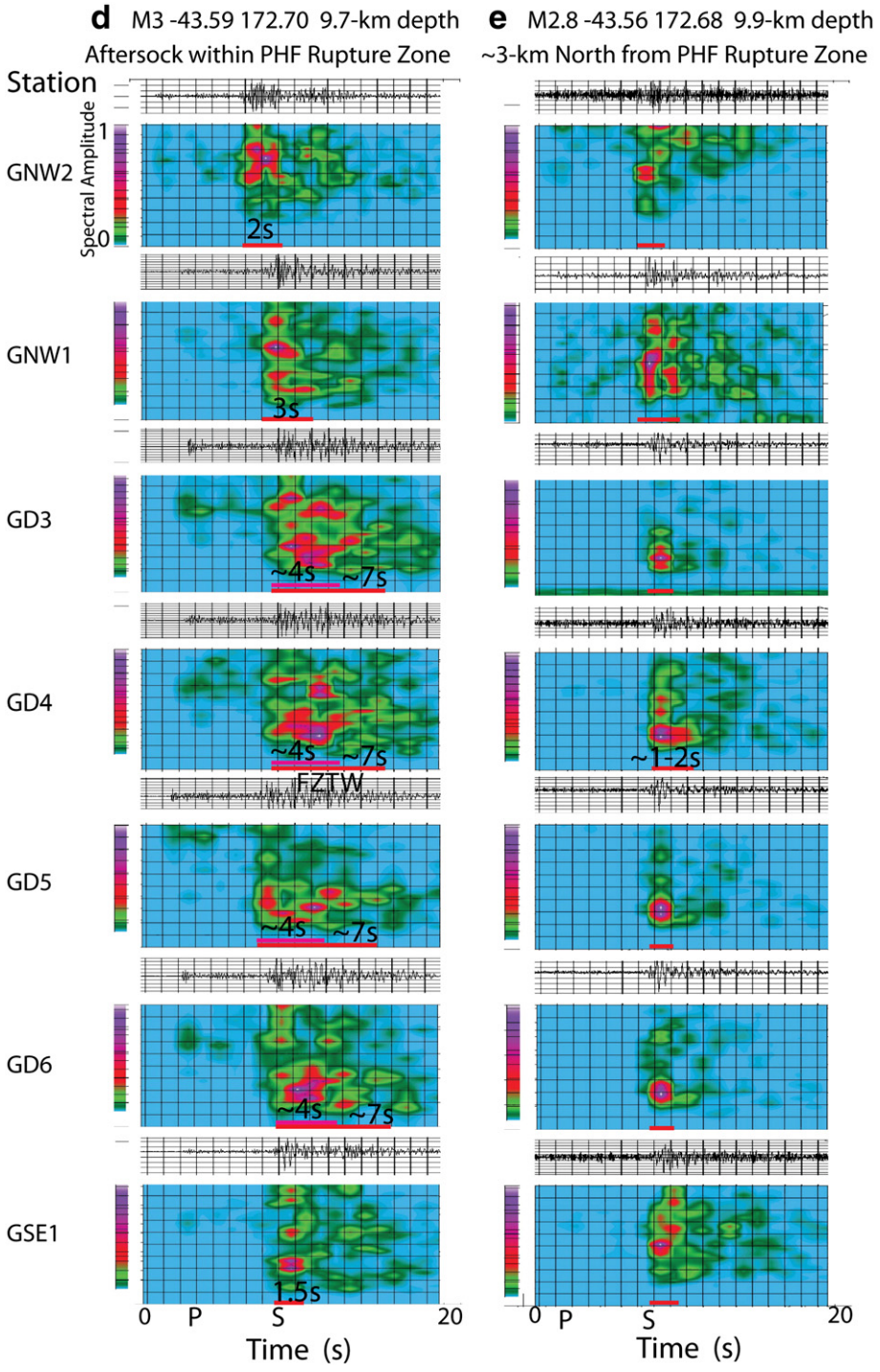

Fig. 8 (*continued*).

We note that the post-S durations of FZTW wavetrains increase as travel distances along the PHF rupture zone increase, but with a relatively smaller increasing trend than the trend along the GF rupture zone, suggesting that rocks within the GF rupture zone might experience greater damage (with the greater seismic velocity reduction) in the 2010 M7.1 Darfield than rocks within the PHF rupture zone did in the 2011 M6.3 Christchurch earthquake. The greater damage magnitude of fault-zone rocks is likely caused by the larger co-seismic slip. This relationship has been reported in previous studies at rupture zones of the 2008 M8 Sichuan earthquake (Li et al., 2012a, 2012b), the 1992 M7.4 Landers and 1999 M7.1 Hector Mine earthquakes (Li et al., 1998, 2003; Vidale and Li, 2003), and 2004 M6 Parkfield earthquake (Li et al., 2006, 2007).

In Fig. 12c, we show the measurements of post-S durations for ~850 aftershocks recorded at Array 1 during our experiment from May to September of 2011. In general, aftershocks occurring far away (~3 km) from the rupture zones show brief body waves with obviously shorter wavetrains than the FZTWs generated by aftershocks occurring within the rupture zone. Ratios of the post-S wavetrain duration time to the P-to-S time for those far off-fault events are much smaller than 1.2. However, for the aftershocks occurring not too far away (less than ~1–1.5 km, ~5 times the wavelength of the dominant FZTWs) from

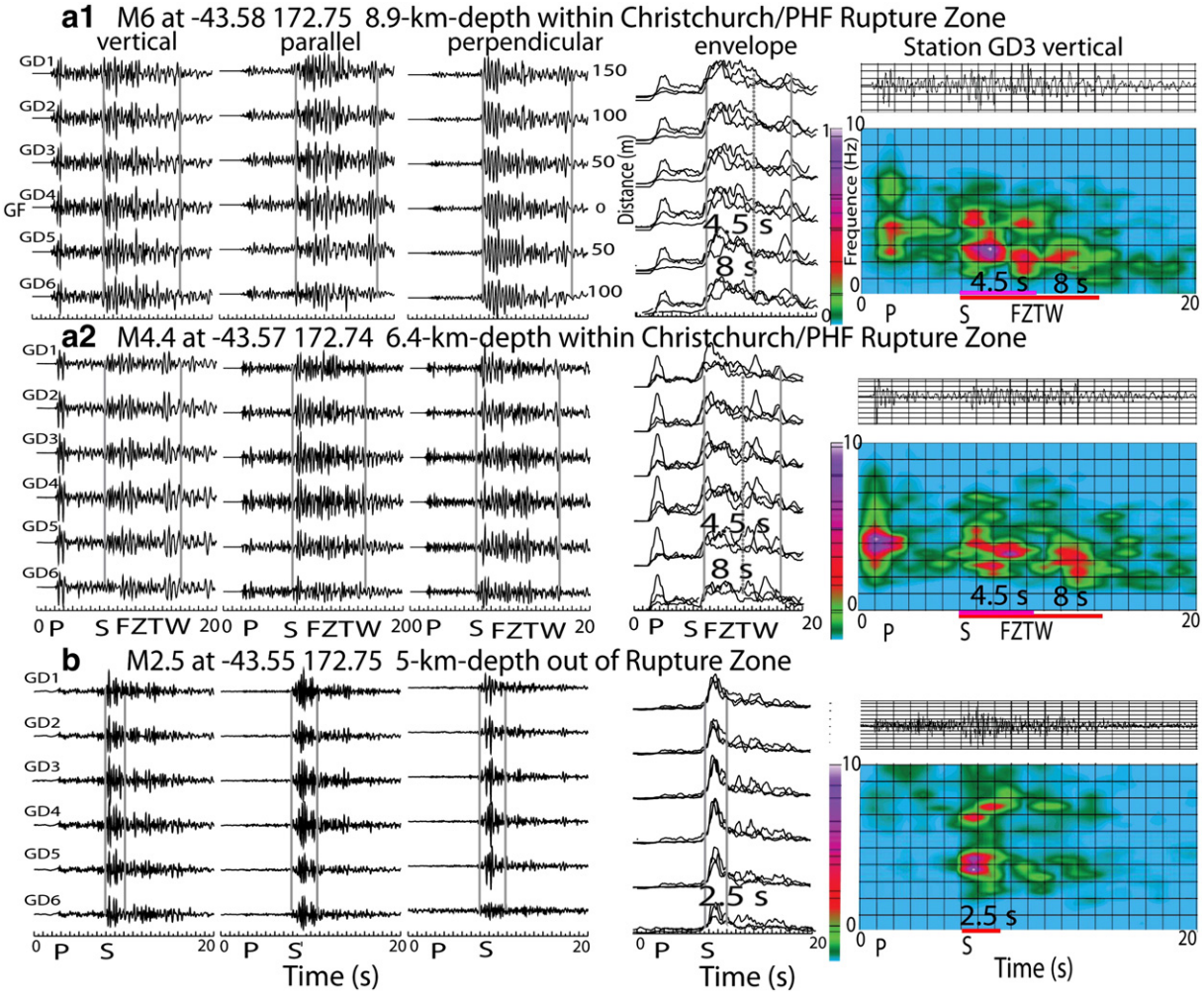

Fig. 9. (a) Three-component seismograms and amplitude envelopes for the 13 June M6 aftershock and its M4.4 aftershock occurring on the east PHF, ~42 km east of Array 1 show ~8.5-s entire post-S durations of FZTWs with the early phase of ~4.5-s in amplitude envelopes and spectral energy. Here, we plot normalized spectral energy at station GD3 only. (b) In contrast, much shorter (~2.5-s) S-waves are dominant in seismograms for the M4.4 off-fault aftershock ~4-km north of the rupture zone.

the rupture zone, a part of seismic energy generated by these events could be trapped by the low-velocity rupture zone, and usually in appearance with relatively shorter wavetrains than the FZTWs generated by aftershocks occurring at the similar longitude but within the low-velocity rupture zone. For these events not far away from the fault, the measured post-S wavetrain durations (denoted by green color) may close to (even overlap) those (denoted by blue and red color) for on-fault aftershocks (seen in Fig. 12c), but the ratio of post-S duration to the P-to-S time is still less than 1.2 (the criteria set for distinguishing significant FZTWs in this study) due to their slightly longer hypocentral distance than on-fault aftershocks at similar longitude, or caused by the heterogeneity of the rock damage along the rupture zone and location errors of the aftershocks. Particularly the measurements of this ratio for aftershocks occurring in the fault step-over and around the NNW-SSE–striking rupture segment north of the central GF are scattered due to rupture branching and the complexity of fault matrix.

3. Subsurface damage structure viewed with FZTWs

Since observations of significant FZTWs is strongly dependent on the source location with respect to the low-velocity waveguide (e.g. Ben-Zion, 1998; Li and Leary, 1990; Li and Vidale, 1996), locations of these aftershocks showing prominent FZTWs allow us to delineate the geometry of subsurface rupture zone with severely damaged rocks, which forms a low-velocity waveguide that traps seismic waves. In this section, we use the aftershocks in Fig. 12 to document the complicated subsurface rock damage structure along multiple faults associated with multiple slips in the 2010 M7.1 Darfield and 2011 M6.3 Christchurch earthquake sequence. Fig. 13a is a map view to show locations of ~230 aftershocks, for which we observed significant FZTWs with the ratio of the duration time of FZTWs to the P-to-S time larger than 1.2. Fig. 13b shows locations of these aftershocks in a 3-D volume. Locations of these aftershocks delineate the subsurface geometry of a low-velocity waveguide along multiple rupture segments composed by severely damaged rocks associated with the Canterbury earthquake sequence. Because we observed prominent FZTWs at Array 1 across the central GF for aftershocks occurring on the GF and the PHF, it requires an effective low-velocity waveguide from the GF through the step-over to the PHF at depth. Otherwise, FZTWs generated by the aftershocks on the PHF could be disrupted by the discontinuity of waveguide at the fault step-over.

Locations of aftershocks generating prominent FZTWs delineate a NNW–SSE-striking rupture segment north of the central GF (Fig. 13a). This segment has an orientation and focal mechanisms that are identified by Sibson et al. (2011) as that expected for newly formed ductile shears in the current stress regime. This rupture segment is consistent with the NNW-striking left-lateral strike fault in the slip model used by Elliott et al. (2012) for geodetic and InSAR data, but it is not included in the model of fault segmentation given by Beavan et al. (2010). This rupture segment follows the NNW trend of aftershocks north of the

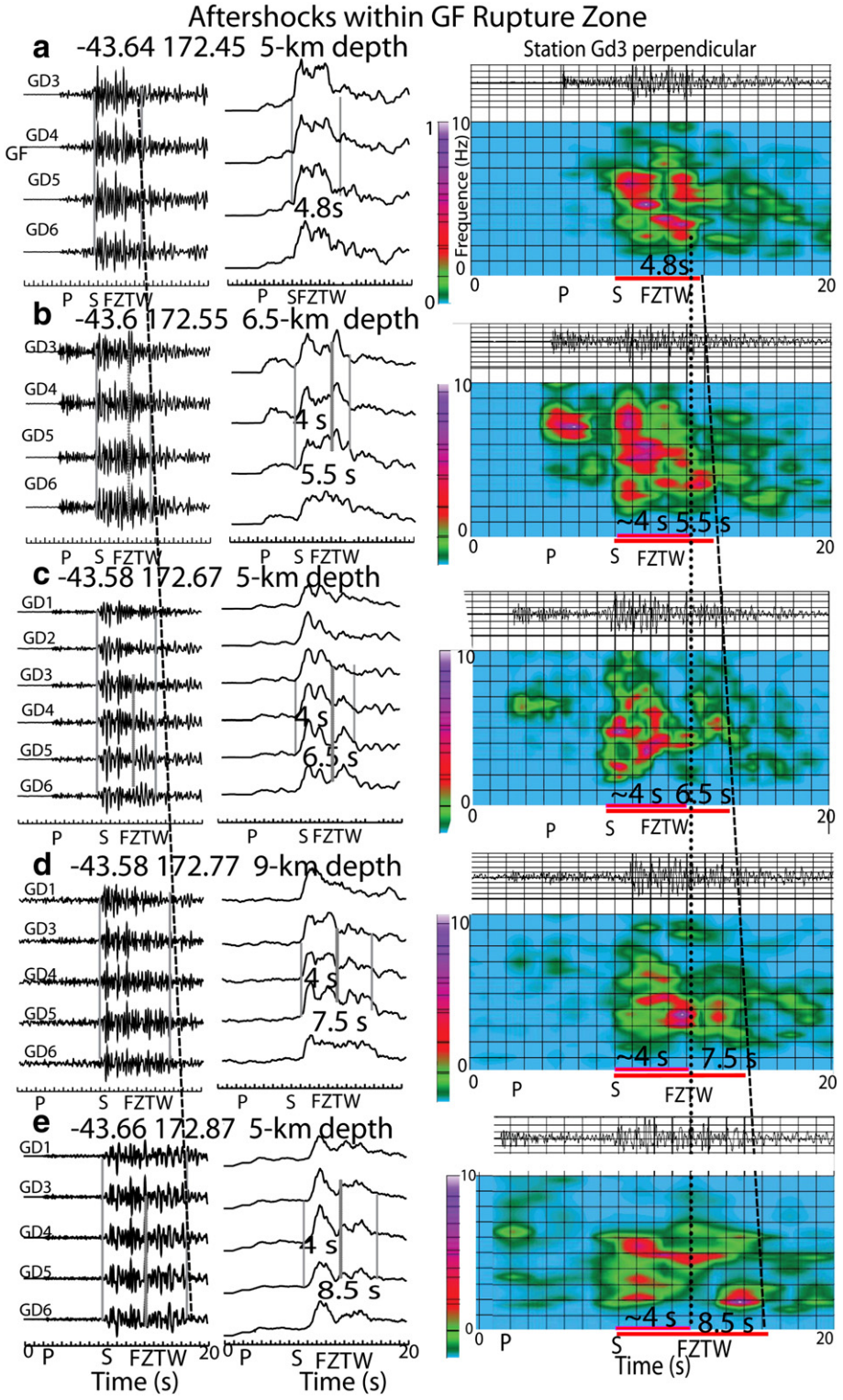

Fig. 10. Perpendicular-component seismograms, amplitude envelopes, and normalized spectral energy registered at central stations of Array 1 within Darfield surface rupture at GF site for 5 aftershocks occurring within the east extension of GF and PHF rupture zones at different depths and epicentral distances. The plots from top to bottom are in the order of increasing hypocentral distances (P-to-S times). The post-S durations of the entire FZTW wavetrains generated by these on-fault aftershocks increase from ~4.8-s to ~8.5-s (measured at 3 near-fault stations GD3, GD4 and GD5) as travel distances of FZTWs increase from ~20-km to ~50-km along the GF and PHF; this move-out is marked by a dash line in seismograms and spectral energy plots. Another vertical dotted line denotes the ~4-s early phase of FZTWs for these aftershocks.

E–W main rupture (Fig. 1). The NNW–SSE band of seismicity extending from the center of the surface rupture to 18 km north of it has been denoted by Syracuse et al. (2013). Based on the seismicity, they interpret that this blind fault dips to the west at an angle that is likely steeper than 65°, with aftershocks from 6.7 to 13.9 km depth. Focal mechanisms calculated for earthquakes along this fault section indicate left-lateral motion (Bannister and Gledhill, 2012; Sibson et al., 2011). Because our Array 1 was located across the E–W central GF east of this NNW–SSE blind strike–slip fault, the FZTWs generated by aftershocks occurring on this fault could arrive at the array. Immediately west of this segment

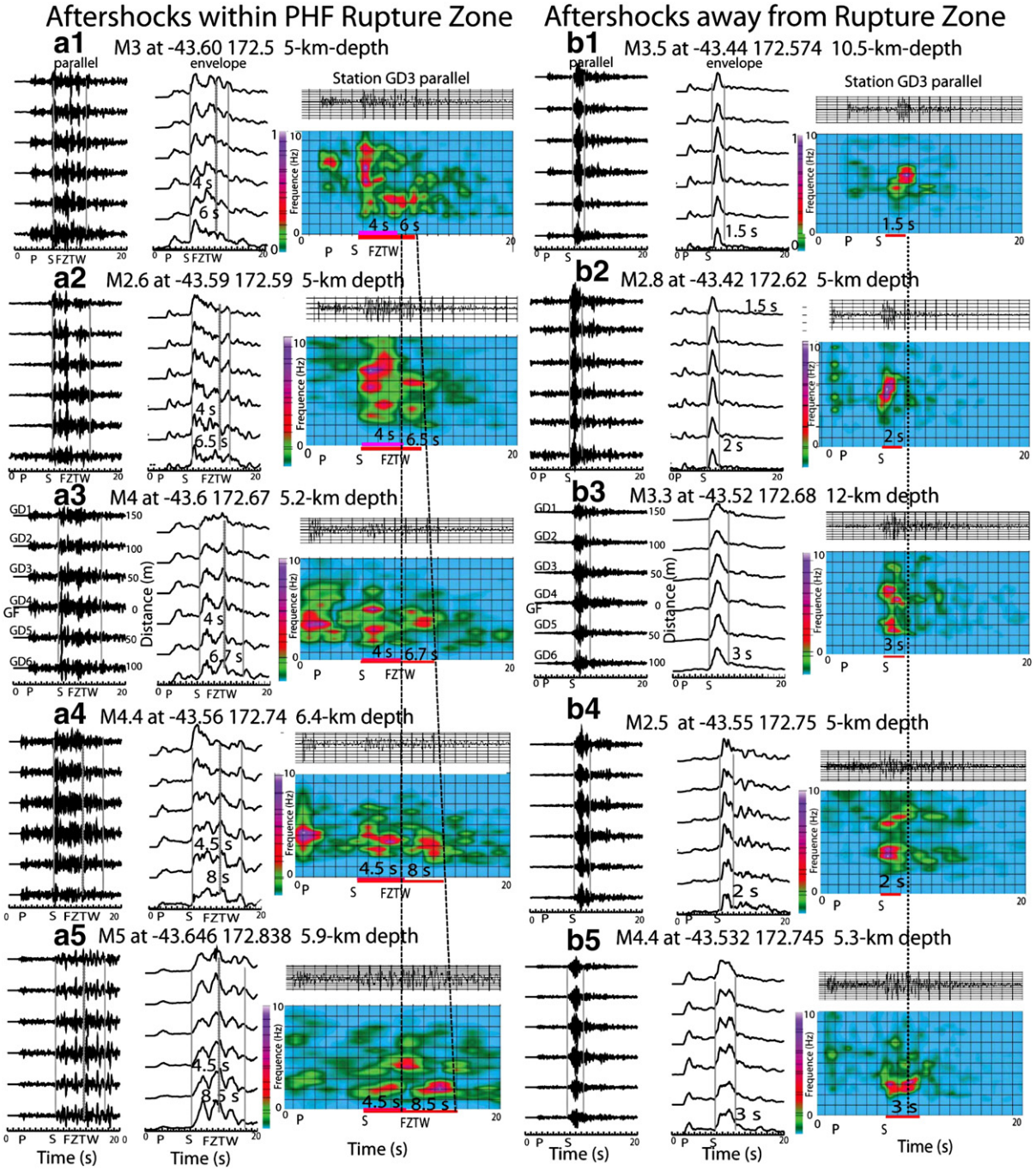

Fig. 11. Parallel-component seismograms, amplitude envelopes, and normalized spectral energy registered at central stations of Array 1 across the GF surface rupture (left) 5 on-fault aftershocks occurring within PHF rupture zone at different depths and epicentral distances and (right) 5 off-fault aftershocks occurring at similar depths and epicentral distances as those on-fault aftershocks. The plots from top to bottom are in the order of increasing hypocentral distances (P-to-S times) of these aftershocks. Post-S durations of FZTWs for 5 on-fault aftershocks increase from ~6-s to ~8.5-s as travel distances increase (the move-out is marked by a dash line) while the early phase of FZTWs remains ~4-4.5-s. In contrast, brief wavetrains of S-waves with much shorter duration ~2–3-s and flat changes (denoted by a vertical dot line) are registered at the same stations for 5 aftershocks away from the rupture zone.

near the center of the GF surface rupture is the Charing Cross blind thrust that was identified by Beavan et al. (2010) as the fault on which the Darfield earthquake initiated. However, all relocated aftershocks (Syracuse et al., 2013) are either beneath the GF surface rupture or along the NNW-striking fault but not along the NNE–SSW Charing Cross Fault. If the FZTWs were generated by aftershocks on the Charing Cross fault, these waves could be disrupted in the intersection with the GF at a NNE angle unfavorable for their propagation to Array 1 across the GF east of the Charing Cross fault.

The rupture segment of the 13 June M6 aftershock viewed by FZTWs seems to occur along a NNW–SSE blind fault confined by the aftershock lineament southeast of Christchurch (Kaiser et al., 2012; Sibson et al., 2011). Because FZTWs (with the ratio of the post-S duration to the P-to-S time smaller than 1.2) generated by those aftershocks traveled long distances to Array 1 at the central GF and along multiple faults, the geometry of the 13 June rupture segment is not delineated as well as the Darfield and Christchurch rupture segments.

4. 3-D finite-difference simulations of observed FZTWs

Based on the complex geometry pattern of multiple rupture segments beneath Canterbury Plains viewed by FZTWS shown in Fig. 13,

we constructed a plausible velocity structure model in 3-D consisting of multiple rupture segments along the GF and PHF (Fig. 14). The layer depths, fault dip, and velocities of surrounding basement rocks are in general constrained by existing models (e.g. Eberhart-Phillips and Bannister, 2002; Elliott et al., 2012; Kaiser et al., 2012; Smith et al., 1995). Velocities and attenuation Q values in this multi-layer model are depth dependent because increasing pressure with increasing depth influences discontinuity density, fluid pressure, and amount of fluids, as well as the healing rates of damaged rocks caused by earthquakes (Byerlee, 1990; Rice, 1992; Sibson, 1996, 2000). The depth-dependent pressure increase may also influence the development of fault gouge (Marone, 1998; Scholz, 1990). For all these reasons, a realistic fault zone is not uniform with depth. Our simulations are based on geometries of rupture segments imaged using locations of aftershocks showing prominent fault-zone trapped waves (Fig. 13). Fig. 14 shows depth sections perpendicular to three rupture segments in our 3-D model: (a) the 250-m-wide Darfield rupture segment along the central GF exposed at the surface, within which velocities are reduced by 35–55% from wall-rock velocities with the maximum reduction in the 100-m fault damage core zone at shallow depth (see model parameters in Table 2), (b) the rupture segment with moderate velocity reduction beneath the surficial fault step-over, and (c) the Christchurch rupture segment along the blind Port Hills fault dipping to SSE at ~70°. This structure most effectively traps 2- to 8-Hz seismic waves. Q values in the model are also depth-dependent, in the range of 20–80 within the rupture zone and 50–200 in basement rocks at depths between 0 and 15 km.

We used a 3-D finite-difference code to compute synthetic seismograms to fit FZTWs recorded at Array 1 across the central GF. The 3D finite-difference computer code used in numerical simulations of FZTWs is second order in time and fourth order in space (Graves, 1996; Vidale et al., 1985). It propagates the complete wave-field through elastic media with a free surface boundary and spatially variable anelastic damping (an approximate Q). The calculation used a 1600-by-600-by-300 element grid in x–y–z coordinates with the grid spacing of 50 m to simulate a volume of 20 km in width, 80 km in length, and 15 km in depth (see Fig. 14). The low-velocity waveguide composed of a fault core zone with maximum velocity reduction sandwiched by a wider damage jacket with milder velocity reduction is embedded in the higher-velocity surrounding rocks with a free surface where the receiver array is placed across the waveguide along the rupture zone. A double-couple source (according to the mainshock focal mechanisms on the GF and the PHF) with radiation patterns was included in the volume.

We simulated the FZTWs recorded at Array 1 for aftershocks occurring at different depths and epicentral distances in a forward-modeling procedure of trial-and-error to obtain the best-fit model parameters. Previous articles on modeling of trapped waves observed at the Parkfield San Andreas fault zone and Landers-Hector Mine rupture zones in California (e.g. Li et al., 2000, 2002, 2004, 2008, 2012a, 2012b) have shown the sensitivity of model parameters to synthetic trapped waveforms with wider fault zones producing trapped waves with lower frequencies, and a slower fault zone producing longer dispersive trapped wave trains. A lower-Q fault zone produces trapped waves with smaller amplitudes and shorter wave trains at lower frequencies. The variation of wall-rock velocities and layer depths affects the arrival times of P and S waves, but variation of wall-rock Q produces minimal variation in modeling results.

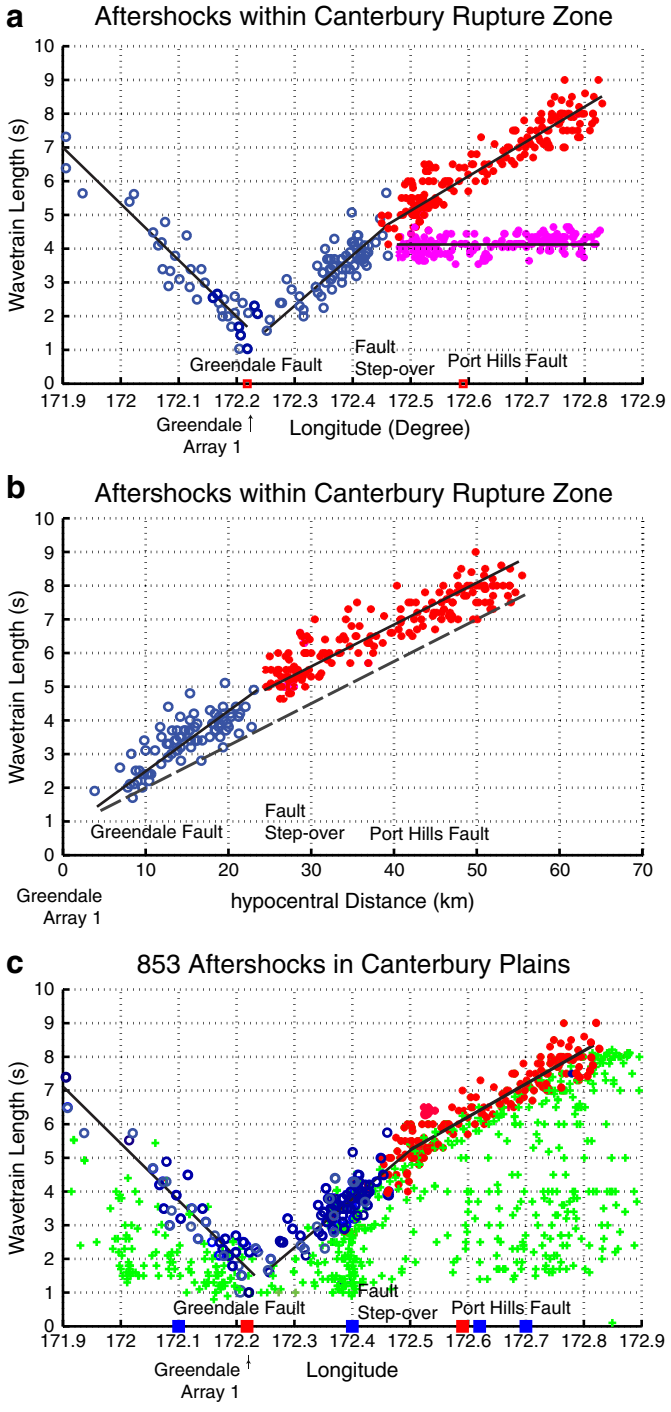

Fig. 12. (a) Measured post-S durations of FZTW wavetrains generated by ~80 aftershocks (denoted by blue circles) occurring within Darfield/GF rupture zone on both sides of Array 1 versus their locations (between longitudes 171.9° and 172.45°) with respect to Array 1, and by ~150 aftershocks (denoted by red dots) occurring within Christchurch/PHF rupture zone versus their locations (between longitudes ~172.45° and 172.83°). Pink dots denote measured post-S durations of early-phase FZTWs for on-PHF aftershocks. Each data point is the average value of post-S durations of FZTWs measured at 3 central stations GD3, GD4 and GD5 of Array 1 within the surface fracturing and folding zone at GF site. These selected aftershocks generated significant FZTWs with the ratio of the entire FZTW wavetrains duration to the P-to-S time greater than 1.2. Solid lines are least-square-fit to measurements. The x-axis in plot is longitude. Red squares denote locations of Array 1 and Array 2. (b) Same as in (a), but the x-axis in plot is hypocentral distances of those on-fault aftershocks, showing the longer post-S duration of FZTWs as these waves travel over a longer distance along the rupture zone. The dashed line fits the P-to-S times by 1.2 * (Ts-Tp). (c) Measured post-S durations for 853 aftershocks recorded at Array 1 during our experiment in Canterbury Plains. Locations of these aftershocks are shown in Fig. 2a. Other notations are same as in (a). Green crosses denote measurements for aftershocks with the ratio of post-S duration to P-to-S time smaller than 1.2. In general, those aftershocks occurred out of rupture zones. Some of them overlap on blue and red circles (see discussion in the text). Four blue squares from left along x-axis denote longitudes of cities of Darfield, Rolleston, Christchurch and Lyttelton.

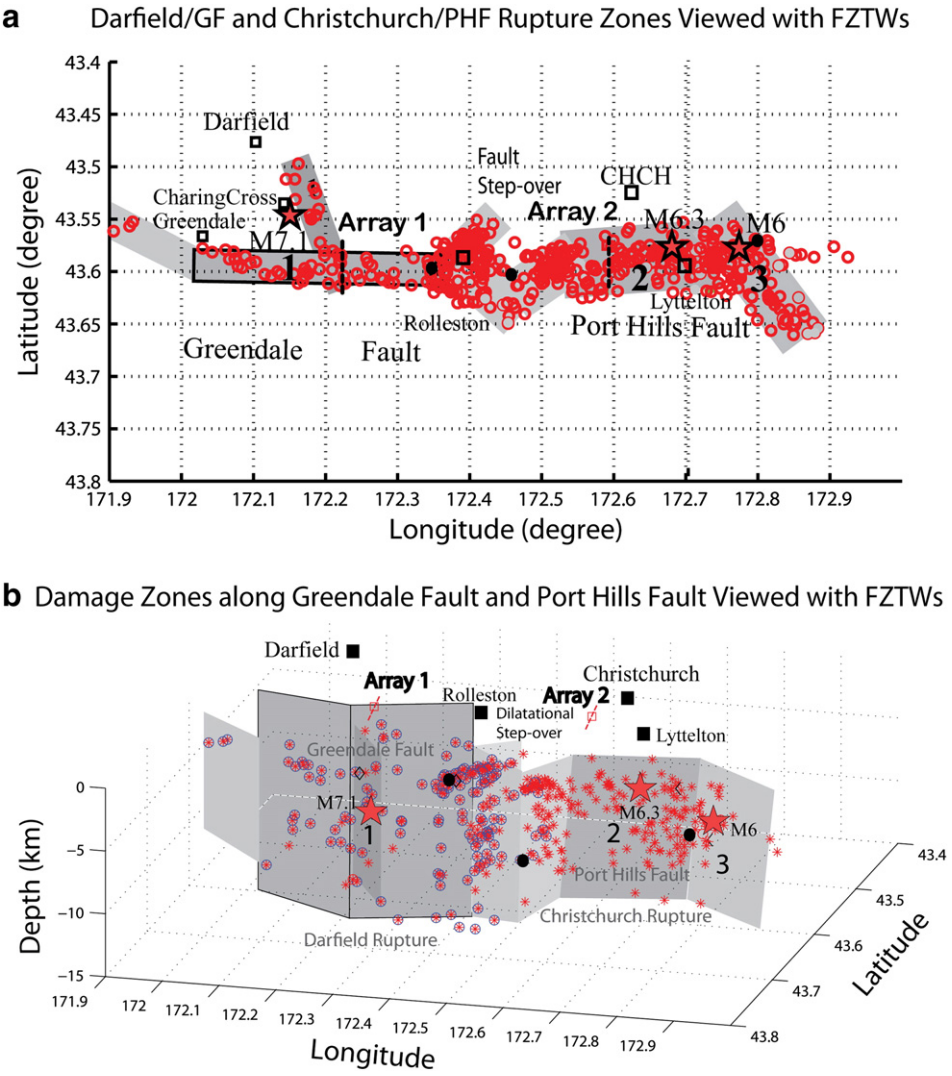

Fig. 13. (a) Map view of locations of ~230 aftershocks (red circles) occurring along the GF and the PHF in Canterbury Plain, for which prominent fault-zone trapped waves (FZTWs) were recorded at Array 1 (marked by a dash line) across the Darfield/GF surface rupture. Locations of these aftershocks delineate the geometry of low-velocity waveguide along multiple rupture segments formed by damaged rocks at depth. Gray bands numbered by 1, 2 and 3 denote rupture zones of the 2010 M7.1 Darfield earthquake, 2011 M6.3 Christchurch earthquake and the June M6 aftershock (marked by 3 stars). The gray band with black edges denotes the rupture segment along the vertical GF exposed at the ground surface. The gray bands without black edges denote blind rupture segments. The blind rupture segment north of the central GF viewed by aftershocks generating significant FZTWs runs along the NNW–SSE-striking left-lateral strike-slip fault indicated by InSAR data (Elliott et al., 2012). The eastward bifurcating extension of the central Darfield rupture zone and the westward extension of Christchurch rupture zone (marked by light gray bands) approach each other beneath the surficial step-over between the GF and PHF. The rupture segment of the June 13th M6 event delineated by FZTWs generated by its aftershocks is along the SE-striking blind fault conjugated to the central PHF. Black squares denote cities and towns in Canterbury Plain. (b) Locations of ~230 aftershocks the same as in (a), for which significant FZTWs were recorded at Array 1 at Highfield road along the GF (marked by red square with dash line), are shown in a 3-D. Locations of these aftershocks delineate the geometry of multiple subsurface rupture segments (marked by gray rectangular boxes) associated with the 2010 – 2011 Canterbury earthquake sequence. The aftershocks denoted by red asterisks with blue circles confine the GF rupture zone (numbered by 1) of the 2010 M7.1 earthquake. The aftershocks denoted by red asterisks confine the PHF rupture zones (numbered by 2 and 3) of the 2010 M6.3 earthquake and the 2011 June M6 aftershock. The central Christchurch rupture segment along the PHF dips to SSE (Bannister et al., 2011). The gray box with black edges denotes the 30-km-long central GF surface rupture exposed at the surface. Gray boxes without black edges denote blind rupture segments. The dark gray box delineates the rupture on a thrusting blind fault on which the 2010 M7.1 Darfield mainshock initiated. The east extension of GF rupture segment and the west extension of PHF rupture segment (denoted by light grey boxes) approach each other beneath the surficial fault step-over, in which rocks were moderately damaged in the Canterbury earthquake sequence. 3 black circles denote aftershocks for which observed and synthetic seismograms are shown in Fig. 15.

Fig. 15a exhibits synthetic waveforms using the model in Fig. 14 to compare with the seismograms at Array 1 for a M2.5 aftershock occurring within the central Darfield/GF rupture segment (depth section (a) in the model) at 5-km depth and 10-km east of Array 1. FZTWs with large amplitudes and ~3-s post-S duration appearing at near-fault stations of Array 1 within the 250-m-wide rupture zone at the GF site, show a remarkable low-velocity waveguide formed by severely damaged rocks along the central GF that ruptured in the 2010 M7.1 Darfield earthquake. The synthetic waveforms in general match observed seismograms, although the fitting degrees are slightly different in three components, probably due to the effects of rock anisotropy (Syracuse et al., 2012) and/or source radiation. Because our finite-difference code is for isotropic media, the effects of rock anisotropy effects cannot be evaluated in this present study.

In the following examples, Fig. 15b exhibits synthetic waveforms using the model in Fig. 14 to fit seismograms recorded at Array 1 for an aftershock occurring at 8.8-km depth and ~20-km east of the GF site within the east extension of GF rupture zone beneath the surficial fault step-over between the GF and PHF (depth section (b) in the model). The synthetic FZTW wavetrains following S-arrivals at stations within the rupture zone show large amplitudes and ~5.5-s duration with a ~4-s early-phase are, in general, agreeable with observations. We note that the FZTWs are composed of two successive phases in wavetrains due to the heterogeneity of the waveguide in geometry

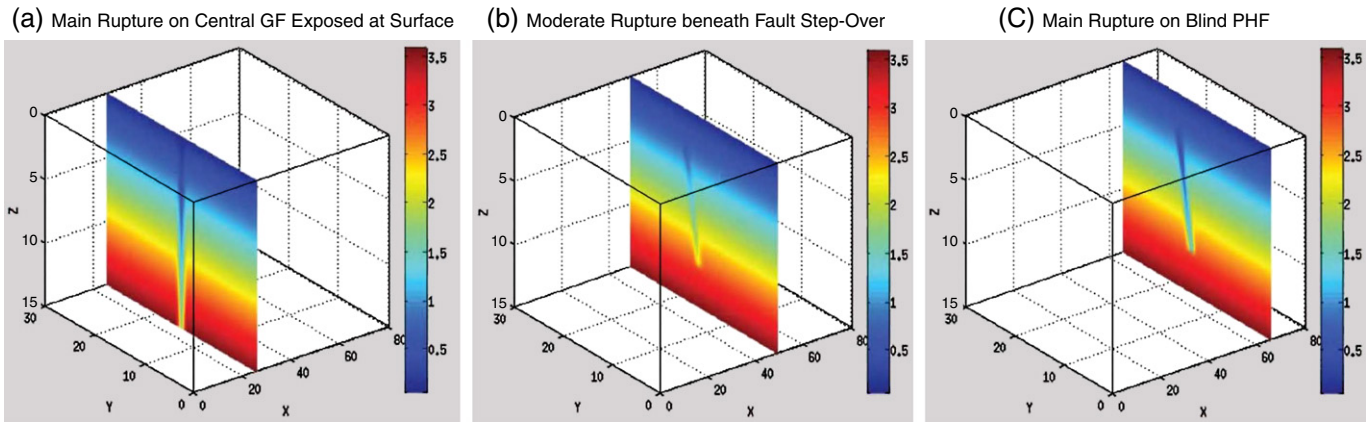

Fig. 14. The rupture zone model and S-wave velocity structures along the central GF ruptured in the M7.1 Darfield earthquake and along the PHF ruptured in the M6.3 Christchurch earthquake in a 3-D volume. This model is used to compute synthetic seismograms to match FZTWs recorded at Array 1, using a 3-D finite-difference code. The low-velocity waveguide along rupture zones is 250-m wide and includes a ~100-m-wide fault core zone. The velocities vary with depth and along rupture zones in this multiple-layer model (see Table 2). The velocities of surrounding rocks are constrained by the velocity models resulted from previous seismic study in Canterbury Plains (see references cited in the text). The color bar is coded with S-wave in km/s. The x-axis is along the fault line in kilometer. The y-axis is perpendicular to the fault line in kilometer. The z-axis is depth in kilometer. Array 1 is located at 25-km from the origin in x-axis and the center of the GF rupture zone at the surface. (a) The depth section perpendicularly across the central GF rupture. The vertical rupture zone is exposed at the surface. Velocities within this rupture segment are reduced by 30–55% from wall-rock velocities, with the maximum reduction with the damage core zone. Model parameters of this section are shown in Table 2. (b) The depth section across the rupture segment with moderate velocity reduction within the waveguide in the fault step-over zone. The rupture zone is blind and dips at 70°. Velocity reductions in this rupture segment are less by ~20% than those in (a). (c) The depth section across PHF rupture segment. The rupture zone is blind and dips at 70°. Velocity reductions in this rupture segment are less by 10% than those in (a). The length of rupture zones are consist with those in Fig. 13. The blind ruptures zones in models are beneath the depth of 2-km.

and with less trapping efficiency beneath the fault step-over where rocks are damaged moderately in the 2010–2011 Canterbury earthquake sequence.

Fig. 15c illustrates a 3-D finite-difference in synthetic waveforms using the model in Fig. 14 to fit seismograms recorded at Array 1 for an aftershock occurring at 7.5-km depth within the PHF rupture segment (depth section (c) in the model), ~45 km west of the GF site. The synthetic waveforms show large amplitude and ~8-s post-S duration with a ~4-s early-phase, in general, agreeable with FZTWs recorded at stations within the 200–250-m-wide rupture zone at the GF site. The entire length of FZTW wavetrains from the aftershock at the greater (~45-km) distance in this example is longer than that from the aftershock at a shorter (~20-km) distance to Array 1 shown in Fig. 15a, indicating that an effective low-velocity waveguide extends from the GF rupture segment to the PHF rupture segment. However, the early-phase FZTWs for these two aftershocks occurring on the GF and the PHF, respectively, show similar durations (~4-s) of the early phase of FZTWs, suggesting that the waveguide has an obvious heterogeneity beneath the step-over between the GF and PHF.

Table 2
Model Parameters for Darfield–Christchurch Rupture Zones.

Model parameters	Layer 1	Layer 2	Layer 3	Layer 4	Layer 5
Depth of the layer bottom, km	2.0	5.0	8.0	12.0	15.0
Waveguide width, m (Damage zone/core)	250/100	250/100	250/100	200/100	100/50
For the Central Darfield/GF rupture zone:					
Waveguide *S* velocity, km/s	1.0/0.5	1.5/1.0	2.0/1.35	2.3/1.8	2.65/2.3
Waveguide *P* velocity, km/s	1.8/1.1	3.0/2.0	4.0/2.7	4.5/3.1	5.0/3.25
For the rupture zone beneath fault step-over:					
Waveguide S velocity, km/s	1.1	1.8/1.2	2.4/1.6	2.7/2.2	
Waveguide P velocity, km/s	2.2	3.6/2.4	4.8/3.2	5.4/3.7	
For the Christchurch/PHF rupture zone:					
Waveguide S velocity, km/s	1.1	1.6/1.1	2.2/1.5	2.5/2.0	
Waveguide P velocity, km/s	2.2	3.3/2.2	4.4/3.0	4.9/3.4	
Waveguide *Q*-value	20	30	50	60	80
Wall-rock *S* velocity, km/sec	1.1	2.0	2.7	3.0	3.3
Wall-rock *P* velocity, km/sec	2.2	4.0	5.5	6.2	6.5
Wall-rock *Q*-value	50	80	100	150	200

In above examples of 3-D finite-difference simulations of FZTWs recorded at Array 1 using the best-fit model in Fig. 14 and parameters in Table 2, we permitted ~1–4 km variation in hypocentral distance of the aftershocks used in modeling to allow for location errors in the GEONET Catalog and the lateral heterogeneity along the fault zone. However, in the forward modeling, the model parameters are interdependent, so they are not uniquely determined. This problem has been discussed in previous studies for the delineation of fault zone structure using trapped waves (e.g., Ben-Zion, 1998; Igel et al., 2002; Li and Leary, 1990; Li and Vidale, 1996). When we have independent estimates of some parameters as modeling constraints, such as group velocities and Q-values estimated from the dispersion and attenuation of trapped waves, and results from other techniques, such as seismic tomography and fault-zone drilling in the region of investigation, for example at the San Andreas Fault in California (Hickman et al., 2007), and the Deep Fault Drilling Project on New Zealand's Alpine Fault (Sutherland et al., 2012), this allows trade-offs among the model parameters to be reduced.

5. Discussion

Highly damaged rocks along the GF and PHF caused by the 2010–2011 Canterbury earthquake sequence (CES) produce a significant low-velocity waveguide to trap seismic waves generated by aftershocks as the sources occurred within or close to the waveguide (Figs. 3 to 11). Since FZTWs arise from constructive interference of reflected waves from the boundaries between the low-velocity fault zone and high-velocity surrounding rocks, the amplitude and dispersion feature of FZTWs are sensitive to the geometry and physical properties of the fault zone. The measured post-S durations of FZTWs in this study show that the longer durations corresponding to the longer travel-distances of FZTWs (Fig. 12), indicating an effective low-velocity waveguide formed by severely damaged rocks along the GF and PHF faults that ruptured in the CES. The waveguide is not uniform but varies in its geometry and velocity reduction from one fault to another.

Based on locations of aftershocks showing significant FZTWs (Fig. 13), we interpret that the Darfield rupture zone (represented by a distinct low-velocity waveguide) extends an additional ~5–8 km eastward and westward as blind segments along aftershock lineaments beyond the 30-km long mapped GF surface rupture trace (e.g. Quigley

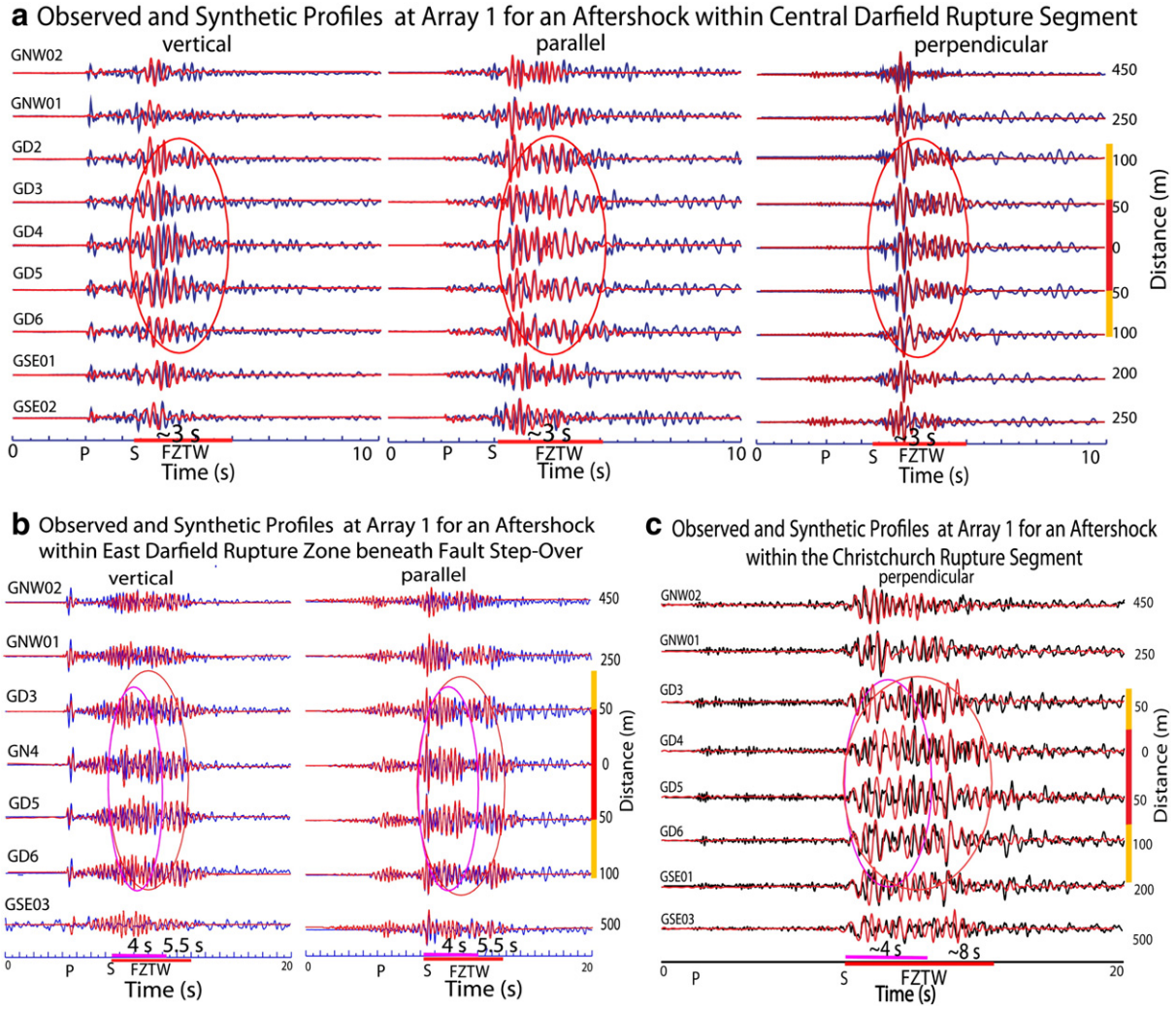

Fig. 15. (a) Three-component 3-D finite-different synthetic waveforms (red lines) compared with seismograms (blue lines) recorded at Array 1 for an aftershock (its location shown in Fig. 13) occurring within the central GF rupture segment at 5-km depth and ~10-km east of Array1. Synthetic seismograms are computed using the model in Fig. 14. Seismograms have been >8 Hz filtered. Fault-zone trapped waves (FZTWs) with large amplitudes and ~3-s post-S duration (denoted by red circles in seismogram and horizontal red bars on the x-axis) appear at stations within the 250-m-wide rupture zone with its ~100-m-wide fault core zone (denoted by vertical yellow and red bars) at Array 1. (b) Vertical- and parallel-component 3-D finite-different synthetic waveforms (red lines) compared with seismograms (black lines) recorded at Array 1 for an aftershock (its location shown in Fig. 13) occurring at 8.8-km depth and ~20-km east of Array 1 within the easternmost extension of the GF rupture beneath the surficial fault step-over between the GF and PHF. Prominent FZTWs show large amplitudes and ~5.5-s post-S duration (denoted by red circles in seismogram and long horizontal red bars on the x-axis), with an early phase with ~4-s post-S duration denoted by pink circles in seismogram and short horizontal pink bars in the x-axis in the entire wavetrains due to the heterogeneity of the waveguide in its geometry and trapping efficiency beneath the fault step-over. (c) 3-D finite-difference synthetic vertical-component waveforms (red) fit seismograms (black) recorded at Array 1 for an aftershock (its location shown in Fig. 13) within the PHF rupture zone at depth 7.6 km and ~45 km west of the array. FZTWs with large amplitude and ~8-s post-S duration (denoted by a red circle in seismograms and a long horizontal red bar in x-axis) appear at stations within the 200–250-m-wide rupture zone along the GF. We note the early-phase FZTWs with ~4-s duration (denoted by a pink circle and a short horizontal pink bar) in all the wavetrains.

et al., 2010). The low-velocity waveguide along the Christchurch rupture zone extends ~15–20-km along the blind central PHF and further westward along aftershock lineaments (Bannister et al., 2011; Syracuse et al., 2013) approaching the east extension of the GF rupture segment beneath the surficial step-over between the GF and the PHF. The rupture length along the PHF viewed with FZTWs is longer than the Christchurch fault plane used in the slip distribution model for inversion of teleseismic, field mapping, SAR and InSAR data (Beavan et al., 2011; Elliott et al., 2012; Holden et al., 2011). It is because the low-velocity waveguide imaged by FZTWs includes the presence of fracture zones beneath the fault step-over, which sufficiently 'connects' the GF and the PHF rupture segments to enable the propagation of FZTWs through it.

Combined with previous rupture models for slip distributions in the CES (Barnhart et al., 2011; Beavan et al., 2011; Elliott et al., 2012; Quigley et al., 2012), we constructed a plausible model of subsurface rupture zones associated with the Darfield–Christchurch earthquakes (Fig. 14). Velocities of basement rocks in our model are constrained by the existing regional velocity models in Canterbury Plains (e.g. Eberhart-Phillips and Bannister, 2002; Kaiser et al., 2012; Smith et al., 1995). Our finite-difference simulations of FZTWs generated by aftershocks at different depths and epicentral distances within the Darfield/GF and Christchurch/PHF rupture zones (examples in Fig. 15) using this model show a 200–250-m wide distinct waveguide along the main rupture zones on the GF and PHF extending down to the depth of ~8–10 km or deeper, consistent with hypocentral depths and geodetic fault models (Elliot et al., 2011; Beavan et al., 2010, 2012), within which velocities are reduced by 35–55% from wall rock velocities with the maximum velocity reduction in the ~100-m-wide damage core zone at shallow depth. The width of the GF core damage zone is consistent with the width of the surface deformation zone consisting of discrete fracturing and distributed folding (Quigley et al., 2012; Van

Dissen et al., 2011). The damage magnitude becomes smaller with depth, consistent with the slip distribution models of the Darfield and Christchurch earthquakes (Elliott et al., 2012; Holden et al., 2011). Our observations and 3-D finite-difference simulations of FZTWs recorded at Array 1 across the GF indicate an effective low-velocity waveguide extending ~65 km (between longitudes 172.0° and 172.8°) along the Greendale fault and Port Hills fault under the Canterbury Plains while the waveguide varies in its velocity and geometry along multiple rupture segments viewed by FZTWs.

We note that a ~10–15-km-long surficial slip gap between the GF and PHF is shown in the InSAR data (Beavan et al., 2011; Elliott et al., 2012). However, our modeling of FZTWs demands an effective low-velocity waveguide along the GF and PHF rupture zones at seismogenic depths although the portion of waveguide beneath the surficial fault step-over shows less velocity reduction (~20–35%) and less trapping efficiency than those along the adjacent main ruptures, which eventually distorts waveforms of FZTWs passing it. We interpret that rocks in 'dilatational step-over' area might have experienced moderate damage due to induced slipping and strong shaking in the CES. This fractured zone might be further developed by successive $M \geq 5$ aftershocks occurring there (Syracuse et al., 2013), and led smaller faults within the step-over zone to grow via linkage.

The model shown in Fig. 14 with parameters in Table 2 represents a gross average of the actual rupture zone structure of the 2010 M7.1 Darfield and 2011 M6.3 Christchurch earthquake sequence at seismogenic depths. The actual structure in 3-D will certainly be more complicated. Although our present model is composed of multiple layers and multiple segments, it still needs more constraints on the variations in damage magnitude and extent along the fault strike and with depth due to rupture distributions and stress variations over multiple length and time scales. A systematic numerical simulation procedure with inversion technique (e.g. the full-3D waveform tomography) for FZTWs using more aftershocks at various depths and epicentral distances will allow us to more accurately document subsurface damage structure in Canterbury Plains in true 3-D. We can assume the damage zones of these splay faults in the South Island's transpressional regime were mostly healed due to the long intervals between ruptures. Thus it provides an opportunity to characterize newly developed damage along these faults and provide a base line to monitor damage zone healing over time and relationship to earthquake hazards in the Canterbury region.

5.1. FZTW constraints on crustal structure between the GF and PHF

The PHF rupture zone viewed with FZTWs runs ~15 km along the central blind PHF dipping to SSE and likely extends additional ~8 km westward along the aftershock lineament into a right-stepping 'dilatational' fault step-over zone, approaching the east extension of the GF rupture segment at seismogenic depths. Accumulated moment release was minimal in the fault step-over zone compared by those on the adjacent rupture segments during this earthquake sequence (Elliott et al., 2012; USGS, http://earthquake.usgs.gov/earthquakes/eqinthenews/2010/us2010atbj/finite_fault.php). However, FZTW characteristics indicate moderate structural 'connectivity' between the PHF and GF. We interpret that the intervening 'dilatational step-over' area ("the gap") consists of damaged rocks that experienced induced slipping and strong shaking in the M7.1 Darfield and M6.3 Christchurch earthquakes and other CES earthquakes (e.g., 11 aftershocks with $M \geq 5$), although the structural connectivity between fractures is not as developed as within the PHF and GF rock damage zones. Rock damage in the 'gap' area is interpreted to have produced a waveguide portion with moderate low velocities between the main rupture segments along the GF and PHF. Because we recorded FZTWs at Array 1 across the central GF for aftershocks occurred along both the GF and PHF, we interpret the step-over zone to facilitate the transfer of FZTW between these major faults via a 'fracture mesh' of NW-oriented, SHmax sub-parallel crustal microcracks (Syracuse et al., 2013), NNW-oriented sinistral 'wrench faults' (e.g., Bannister and Gledhill, 2012; Sibson et al., 2011), and E–W striking dextral faults (Fig. 1). We interpret the E–W trending faults as smaller scale analogs of the GF, and suggest that these structures may share a similar Cretaceous history. The fractures in this area seem to be at an incipient stage in their development, with no evidence for large scale fracture connectivity that could facilitate a combined GF-PHF co-seismic rupture through this area. However, we cannot state absolutely that separate structures of sufficient connectivity and length to facilitate larger earthquakes (i.e., ~M6) do not exist in this area. A comparable example in such a case is seen at the Kickapoo fault in the step-over between the Johnson Valley fault and Homestead Valley fault, which ruptured in the 1992 M7.4 Landers earthquake in the Mojave Desert, California (Li et al., 1994, 2000). Focal mechanisms on the westward projection of the PHF suggest a steepening of fault dip to sub-vertical and a transition to almost purely dextral strike–slip (Bannister et al., 2011; Syracuse et al., 2013). Because both faults are likely to be steeply dipping as they approach the step-over zone, we estimate the likely distance between the faults at seismogenic depth by measuring the distance between possible positions of the GF and PHF subsurface extensions as revealed by increased hypocentral and epicentral density compared to 'off-fault' areas. We derive a minimum distance of 3.5 km, a maximum distance of 8.5 km, and a 'preferred distance' of 5.3 ± 1 km for this step-over zone, as measured from the highest density of earthquakes with dextral strike–slip mechanisms with a fault plane consistent with the orientation of the PHF and GF when entering the step-over zone. This distance is consistent with the studies of Wesnousky (2006, 2008) who suggests that a releasing step-over width of 3–4 km should be sufficient to terminate most earthquake ruptures. With progressive earthquake cycling over geological timescales and progressive westward migration of the fault into the more rapidly deforming region of the Australia–Pacific Plate boundary, it is possible that the GF–PHF connectivity may increase to a state where combined GF–PHF ruptures are a possibility. Structurally mature analogs of this system could include the Porter's Pass–Amberley Fault Zone, which shows evidence for both segmented rupture behavior in Mw 7.1–7.4 earthquakes and wall-to-wall rupture behavior through segments in Mw7.5–7.7 earthquakes (Howard et al., 2005).

While we have identified FZTWs in seismograms recorded at Array 1 for aftershocks occurring within the rupture zones along the GF and PHF, we did not observe significant FZTWs in seismograms recorded at Array 2 for these aftershocks. The Permian to Early Cretaceous 'Torlesse' greywacke basement terrain beneath the Canterbury Plains and Port Hills is variably overlain by 1–2 km of Cretaceous to Neogene sedimentary and volcanic rocks and 0–1 km of unconsolidated Quaternary sediments (Forsyth et al., 2008). The geodetically modeled 'top' of the PHF rupture zone at approximately 50–0 m to 1-km depth below surface (Beavan et al., 2012) is likely to terminate in or below the Miocene volcanic rocks of the Banks Peninsula and/or post-Cretaceous sedimentary rocks. Conversely, the GF ruptured from basement rocks through Quaternary gravels to the surface (Quigley et al., 2012). Both the PHF and GF are likely to be reactivated Cretaceous rift faults, given the presence of analogous structures visible in the rifted Chatham Rise offshore. Thus the fault damage zone in the hypocentral and centroid areas of these faults is likely to reflect reactivation of pre-existing crustal anisotropy (Holt et al., 2013). However, the PHF rupture is likely overlain both by volcanic and sedimentary rocks with shallowly-dipping layering (e.g., volcanic flow layers, sedimentary bedding) at a high angle to the fault zone and seismic wave ray path that would have disrupted and/or attenuated PHF guided waves in the region between the top of the fault and the surface seismic array. Li and Vidale (1996) have numerically shown the effect of the unbroken surface layer which may distort and attenuate FZTWs. They illustrated that the closer the low-velocity fault zone is to the surface, the more clearly fault-zone trapped waves are recorded on the surface fault trace. Seismograms we recorded at Array 1 across the GF surface rupture where the low-velocity waveguide formed by severely damaged rocks at depths are

transmitted to the ground surface through ~750 m of Quaternary gravels and demonstrate that the waveguide trapping effect is not dissipated by thick sedimentary deposits.

Our experiment also illuminates a potential approach to image the sub-surface portion of a rupture zone using FZTWs recorded at seismic arrays deployed along a surface rupture. This approach may be useful for investigation of fault rupture zones in urban areas where the deployment of seismic arrays are difficult, instead we can record FZTWs along seismic arrays deployed along sections of the same fault in rural areas where access is oftentimes easier to obtain.

Acknowledgments

This material is based upon work supported by the National Science Foundation under Grants EAR-1142071 and EAR-1137632, and the Southern California Earthquake Center (contribution number 1764). We are grateful to Reviewer M. Savage for her helpful comments to this manuscript and P. Malin, C. Thurber, H. Cowan, K. Berryman, T. Jordan, J. Pettinga, and J. McRaney for their helpful discussions about our experiment in the Canterbury Plains in NZ South Island. Thanks to Matt Cockcroft for equipment support at the University of Canterbury. We acknowledge the IRIS for the use of PASSCAL instruments in our RAMP experiment in New Zealand. Thanks to J. Cherrington and M. Alvarez for their participation in early deployment of seismographs in the field. Special thanks to the local landowners in Canterbury for allowing us to install seismic stations on their land.

References

Aki, K., 1984. Asperities, barriers, characteristic earthquakes, and strong motion prediction. J. Geophys. Res. 89, 5867–5872.

Bannister, S., Gledhill, K., 2012. Evolution of the 2010–2012 Canterbury earthquake sequence. N.Z. J. Geol. Geophys. 55 (3), 295–304. http://dx.doi.org/10.1080/00288306.2012.680475.

Bannister, S., Fry, B., Reyners, M., Ristau, J., Zhang, H., 2011. Fine-scale relocation of aftershocks of the 22 February Mw 6.2 Christchurch earthquake using double-difference tomography. Seismol. Res. Lett. 82 (6), 839–845.

Barnhart, W.D., Willis, M.J., Lohman, R.B., Melkonian, A.K., 2011. InSAR and optical constraints on fault slip during the 2010–2011 New Zealand earthquake sequence. Seismol. Res. Lett. 82 (6), 815–823.

Barrell, D.J.A., Litchfield, N.J., Townsend, D.B., Quigley, M., Van Dissen, R.J., Cosgrove, R., Cox, S.C., Furlong, K., Villamor, P., Begg, J.G., Hemmings-Sykes, S., Jongens, R., Mackenzie, H., Noble, D., Stahl, T., Bilderback, E., Duffy, B., Henham, H., Klahn, A., Lang, E.M.W., Moody, L., Nicol, R., Pedley, K., Smith, A., 2011. Photographic Feature: Strike-slip ground-surface rupture (Greendale Fault) associated with the 4 September 2010 Darfield earthquake, Canterbury, New Zealand. Q. J. Eng. Geol. Hydrogeol. 44, 283–291.

Beavan, R.J., Samsonov, S., Motagh, M., Wallace, L.M., Ellis, S.M., Palmer, N.G., 2010. The Darfield (Canterbury) earthquake: geodetic observations and preliminary source model. Bull. N. Z. Soc. Earthq. Eng. 43 (4), 228–235.

Beavan, J., Fielding, E., Motagh, M., Samsonov, S., Donnelly, N., 2011. Fault location and slip distribution of the 22 February 2011 Mw 6.2 Christchurch, New Zealand, earthquake from geodetic data. Seismol. Res. Lett. V82, 789–799. http://dx.doi.org/10.1785/gssrl.82.6.789.

Beavan, J., Motagh, M., Fielding, E., Donnelly, N., Collett, D., 2012. Fault slip models of the 2010–2011 Canterbury, New Zealand, earthquakes from geodetic data, and observations of post-seismic ground deformation. N. Z. J. Geol. Geophys. 55. http://dx.doi.org/10.1080/00288306.2012.697472.

Beck, S.L., Christensen, D.H., 1991. Rupture process of the February 4, 1965, Rat Islands earthquake. J. Geophys. Res. 96, 2205–2221.

Ben-Zion, Y., 1998. Properties of seismic fault zone waves and their utility for imaging low velocity structures. J. Geophys. Res. 103, 12567–12585.

Blanpied, M.L., Lockner, D.A., Byerlee, J.D., 1992. An earthquake mechanism based on rapid sealing of faults. Nature 359, 574–576.

Byerlee, J., 1990. Friction, overpressure and fault-normal compression. Geophys. Res. Lett. 17, 2109–2112.

Chester, F.M., Evans, J.P., Biegel, R.L., 1993. Internal structure and weakening mechanisms of the San Andreas fault. J. Geophys. Res. 98, 771–786.

Das, S., Aki, K., 1997. Fault plane with barriers: A versatile earthquake model. J. Geophys. Res. 82, 5658–5670.

Davy, B., Stagpool, V., Yu, D., 2012. Subsurface structure of the Canterbury region interpreted from gravity and aeromagnetic data. N. Z. J. Geol. Geophys. 55 (3), 185–191.

Eberhart-Phillips, D., Bannister, S., 2002. Three-dimensional crustal structure in the Southern Alps region of New Zealand from inversion of local earthquake and active source data. J. Geophys. Res. 107. http://dx.doi.org/10.1029/2011JB000567.

Elliott, J.R., Nissen, E.K., England, P.C., Jackson, J.A., Lamb, S., Li, Z., Oehlers, M., Parsons, B., 2012. Slip in the 2010–2011 Canterbury earthquakes, New Zealand. J. Geophys. Res. 117 (B03401), 1–36. http://dx.doi.org/10.1029/2011JB008868.

Ellsworth, W.L., 1990. Earthquake history, 1769–1989. In: Wallace, R.E. (Ed.), The San Andreas Fault System, California. U.S. Geol. Surv. Profess. Pap., 1515, pp. 153–187.

Ellsworth, W.L., Malin, P.E., 2011. Deep rock damage in the San Andreas fault revealed by P- and S-type fault zone guided waves, Sibson's volume. Geological Society Special Publication, V359, pp. 39–53 (New Zealand).

Forsyth, P. J., D. J. Barrell, and R. Jongen, 2008. Geology of the Christchurch Area, Institute of Geological and Nuclear Sciences, 1:250,000 geological map 16, 1 sheet and 67 pp. Lower Hutt, New Zealand: GNS Science.

Gledhill, K., Ristau, J., Reyners, M., Fry, B., Holden, C., 2011. The Darfield (Canterbury, New Zealand) Mw 7.1 earthquake of September 2010: A preliminary seismological report. Seismol. Res. Lett. 82 (3), 378–386. http://dx.doi.org/10.1785/gssrl.82.3.378.

Graves, R.W., 1996. Simulating seismic wave propagation in 3D elastic media using staggered-grid finite differences. Bull. Seismol. Soc. Am. 86, 1091–1106.

Harris, R.A., Day, S.M., 1993. Dynamics of fault interaction: parallel strike–slip faults. J. Geophys. Res. 98, 4461–4472.

Hickman, S.H., Zoback, M.D., Ellsworth, W.L., Boness, N., Malin, P., Roecker, S., Thurber, C., 2007. Structure and properties of the San Andreas Fault in Central California: recent results from the SAFOD experiment, Scientific Drilling, Special Issue, No.1. 29–32. http://dx.doi.org/10.2204/iodp.sd.s01.39.2007.

Holden, C., Beavan, J., Fry, B., Reyners, M., Ristau, J., Van Dissen, R., Villamor, P., 2011. Preliminary source model of the Mw7.1 Darfield earthquake from geological, geodetic and seismic data. Proceedings of the 9th Pacific Conference on Earthquake Engineering Building an Earthquake-Resilient Society, 14-16 April, 2011, Auckland, New Zealand, paper No. 164.

Holt, R.A., Savage, M.K., Townend, J., Syracuse, E.M., Thurber, C.H., 2013. Crustal stress and fault strength in the Canterbury Plains, New Zealand. Earth Planet. Sci. Lett. 383, 173–181.

Howard, M., Nicol, A., Campbell, J., Pettinga, J.R., 2005. Holocene paleoearthquakes on the strike–slip Porters Pass Fault, Canterbury, New Zealand. N. Z. J. Geol. Geophys. 48, 59–74. http://dx.doi.org/10.1080/00288306.2005.9515098.

Igel, H., Jahnke, G., Ben-Zion, Y., 2002. Numerical simulation of fault zone guided waves: accuracy and 3-D effects. Pure Appl. Geophys. 159, 2067–2083.

Jogens, R., Barrell, D., Campbell, J., Pettinga, J., 2012. Faulting and folding beneath the Canterbury Plains identified prior to the 2010 emergence of the Greendale Fault. N. Z. J. Geol. Geophys. 55 (3), 169–176.

Johnson, A.M., Fleming, R.W., Cruishank, K.M., 1994. Shear zones formed along long, straight traces of fault zones during the 28 June 1992 Landers, California earthquake. Bull. Seismol. Soc. Am. 84, 499–510.

Kaiser, A., Holden, C., Beavan, J., Beetham, D., Benites, R., Celentano, A., Collett, D., Cousins, J., Cubrinovski, M., Dellow, G., Denys, P., Fielding, E., Fry, B., Gerstenberger, M., Langridge, R., Massey, C., Motagh, M., Pondard, N., McVerry, G., Ristau, J., Stirling, M., Thomas, J., Uma, S.R., Zhao, J., 2012. The Mw 6.2 Christchurch earthquake of February 2011: preliminary report. N. Z. J. Geol. Geophys. 55 (1), 67–90.

Korneev, V.A., Nadeau, R.M., McEvilly, T.V., 2003. Seismological studies at Parkfield IX: Fault-zone imaging using guided wave attenuation. Bull. Seismol. Soc. Am. 80, 1245–1271.

Li, Y.G., Malin, P.E., 2008. San Andreas Fault damage at SAFOD viewed with fault-guided waves. Geophys. Res. Lett. 35, L08304. http://dx.doi.org/10.1029/2007GL032924.

Li, Y.G., Vidale, J.E., 1996. Low-velocity fault-zone guided waves: numerical investigations of trapping efficiency. Bull. Seismol. Soc. Am. 86, 371–378.

Li, Y.G., Vidale, J.E., 2001. Healing of the shallow fault zone from 1994–1998 after the 1992 M7.5 Landers, California, earthquake. Geophys. Res. Lett. 28, 2999–3002.

Li, Y.G., Leary, P.C., Aki, K., Malin, P.E., 1990. Seismic trapped modes in the Oroville and San Andreas fault zones. Science 249, 763–766.

Li, Y.G., Aki, K., Adams, D., Hasemi, A., Lee, W.H.K., 1994. Seismic guided waves trapped in the fault zone of the Landers, California, earthquake of 1992. J. Geophys. Res. 99, 11,705–11,722.

Li, Y.G., Vidale, J.E., Aki, K., Xu, F., Burdette, T., 1998. Evidence of shallow fault zone strengthening after the 1992 M7.5 Landers, California, earthquake. Science 279, 217–219.

Li, Y.G., Vidale, J.E., Aki, K., Xu, F., 2000. Depth-dependent structure of the Landers fault zone using fault zone trapped waves generated by aftershocks. J. Geophys. Res. 105, 6237–6254.

Li, Y.G., Vidale, J.E., Day, S.M., Oglesby, D., 2002. Study of the M7.1 Hector Mine, California, earthquake fault plan by fault-zone trapped waves, Hector Mine Earthquake Special Issue. Bull. Seismol. Soc. Am. 92, 1318–1332.

Li, Y.G., Vidale, J.E., Oglesby, D., Day, S.M., Cochran, E., 2003. Multiple-fault rupture of the M7.1 Hector Mine, California, earthquake from fault-zone trapped waves. J. Geophys. Res. 108 (ESE 11), 1–25.

Li, Y.G., Vidale, J.E., Cochran, S.E., 2004. Low-velocity damaged structure of the San Andreas fault at Parkfield from fault-zone trapped waves. Geophys. Res. Lett. 31, L12S06.

Li, Y.G., Chen, P., Cochran, E.S., Vidale, J.E., Burdette, T., 2006. Seismic evidence for rock damage and healing on the San Andreas fault associated with the 2004 M6 Parkfield earthquake, Special issue for Parkfield M6 earthquake. Bull. Seismol. Soc. Am. 96 (4), S1–S15. http://dx.doi.org/10.1785/0120050803.

Li, Y.G., Chen, P., Cochran, E., Vidale, J., 2007. Seismic velocity variations on the San Andreas Fault caused by the 2004 M6 Parkfield earthquake and their implications. Earth Planets Space 59, 21–31.

Li, Y.G., Malin, P., Cochran, E., 2012a. Fault-zone trapped waves: high-resolution characterization of the damage zone on the Parkfield San Andreas Fault at depth Chapter 3 In: Li, Y.G. (Ed.), Imaging, Modeling and Assimilation in Seismology. China High-Education Press, Beijing, pp. 107–150 (De Gruyter, Boston, USA).

Li, Y.G., Sue, J.Y., Chen, T.C., 2012b. Fault-zone trapped waves at a dip fault: documentation of rock damage on the thrusting Longmen–Shan fault ruptured in the 2008 M8 Wenchuan earthquake Chapter 4 In: Li, Y.G. (Ed.), Imaging, Modeling and

Assimilation in Seismology. China High-Education Press, Beijing, pp. 151–198 (De Gruyter, Boston, USA).
Malin, P.E., Blakeslee, S.N., Alvarez, M.G., Martin, A.J., 1989. Microearthquake imaging of the Parkfield asperity. Science 244, 557–559.
Marone, C., 1998. The effect of loading rate on static friction and the rate of fault healing during the earthquake cycle. Nature 391, 69–72.
Michael, A.J., Eberhart-Phillips, D.M., 1991. Relationships between fault behavior, subsurface geology, and three-dimensional velocity models. Science 253, 651–654.
Michelini, A., McEvilly, T.V., 1991. Seismological studies at Parkfield. I. Simultaneous inversion for velocity structure and hypocenters using cubic B-splines parameterization. Bull. Seismol. Soc. Am. 81, 524–552.
Mooney, W.D., Ginzburg, A., 1986. Seismic measurements of the internal properties of fault zones. Pure Appl. Geophys. 124, 141–157.
Oglesby, D.D., Day, S.M., Li, Y.G., Vidale, J.E., 2003. The 1999 Hector Mine earthquake: the dynamics of a branched fault system. Bull. Seismol. Soc. Am. 93, 2459–2476.
Quigley, M., Villamor, P., Furlong, K., Beavan, J., Van Dissen, R., Litchfield, N., Stahl, T., Duffy, B., Bilderback, E., Noble, D., Barrell, D., Jongens, R., Cox, S., 2010. Previously unknown fault shakes New Zealand's South Island. EOS Trans. Am. Geophys. Union 91 (49), 469–471.
Quigley, M., Van Dissen, R., Litchfield, N., Villamor, P., Barrell, D., Stahl, T., Bilderback, E., Noble, D., 2012. Surface rupture during the 2010 M_w7 Darfield (Canterbury) earthquake; implications for fault rupture dynamics and seismic hazard analysis. Geology 40 (1), 55–58.
Rice, J.R., 1992. Fault stress states, pore pressure distributions, and the weakness of the San Andreas fault. In: Evans, B., Wong, T.-F. (Eds.), Fault Mechanics and Transport Properties of Rocks. Academic, San Diego, Calif, pp. 475–503.
Scholz, C.H., 1990. The Mechanics of Earthquakes and Faulting. Cambridge Univ, Press, New York.
Shcherbakov, R., Nguyen, M., Quigley, M., 2012. Statistical analysis of the 2010 MW7.1 Darfield Earthquake aftershock sequence. N. Z. J. Geol. Geophys. 55 (3), 305–311 (September 2012).
Sibson, R.H., 1996. Structural permeability of fluid-driven fault-fracture meshes. J. Struct. Geol. 18, 1031–1042.
Sibson, R.H., 2000. Tectonic controls on maximum sustainable overpressure: fluid redistribution from stress transitions. J. Geochem. Explor. 69–70, 471–475.
Sibson, R., Ghisetti, F., Ristau, J., 2011. Stress control of an evolving strike–slip fault system during 2010–2011 Canterbury, New Zealand, earthquake sequence. Seismol. Res. Lett. 82 (6), 824–832.
Sieh, K., Jones, L., Hauksson, E., Hudnut, K., Eberhart-Phillips, D., Heaton, T., Hough, S., Hutton, K., Kanamori, H., Lilji, A., Lindvall, S., McGill, S., Mori, J., Rubin, C., Spotila, J., Stock, J., Thio, H., Treiman, J., Wernick, B., Zachariasen, J., 1993. Near-field investigations of the Landers earthquake sequence, April to July 1992. Science 260, 171–176.
Smith, E.G., Stern, T., O'Brien, B., 1995. A seismic velocity profile across the central South Island, New Zealand, from explosion data. N. Z. J. Geol. Geophys. 38, 565–570.
Sutherland, R., Toy, V.G., Townend, J., Cox, S.C., Eccles, J.D., Faulkner, D.R., Prior, D.J., Norris, R.J., Mariani, E., Boulton, C., Carpenter, B.M., Menzies, C.D., Little, T.A., Hasting, M., De Pascale, G.P., Langridge, R.M., Scott, H.R., Reid Lindroos, Z., Fleming, B., Kopf, A.J., 2012. Drilling reveals fluid control on architecture and rupture of the Alpine fault. N. Z. Geol. 40, 1143–1146.
Syracuse, E.M., Holt, R.A., Savage, M.K., Johnson, J.H., Thurber, C.H., Unglert, K., Henderson, M., 2012. Temporal and spatial evolution of hypocentres and anisotropy from the Darfield aftershock sequence: implications for fault geometry and age. N. Z. J. Geol. Geophys. 55 (3), 287–293.
Syracuse, E., Thurber, C., Rawles, C., Savage, M., Bannister, S., 2013. High-resolution relocation of aftershocks of the Mw 7.1 Darfield, New Zealand, earthquake and implications for fault activity. J. Geophys. Res. 118, 1–12. http://dx.doi.org/10.1002/jgrb.50301.
Thurber, C., Roecker, S., Zhang, H., Baher, S., Ellsworth, W., 2004. Fine-scale structure of the San Andreas fault zone and location of the SAFOD target earthquakes. Geophys. Res. Lett. 31, L12S02. http://dx.doi.org/10.1029/2003GL019398.
Thurber, C., Zhang, H., Waldhauser, F., Hardbeck, J., Michael, A., Eberhart-Phillips, D., 2006. Three-dimensional compressional wavespeed model, earthquake relocations, and focal mechanisms for the Parkfield, California, region. Bull. Seismol. Soc. Am. 96, S38–S49. http://dx.doi.org/10.1785/0120050825.
Van Dissen, R., et al., 2011. Surface rupture displacement on the Greendale Fault during the Mw 7.1 Darfield (Canterbury) earthquake, New Zealand, and its impact on man-made structures. proceedings, 9th Pacific Conference on Earthquake Engineering, NZSEE, Auckland, NZ.
Vidale, J.E., Li, Y.G., 2003. Damage to the shallow Landers fault from the nearby Hector Mine earthquake. Nature 421, 524–526.
Vidale, J.E., Helmberger, D.V., Clayton, R.W., 1985. Finite-difference seismograms for SH waves. Bull. Seismol. Soc. Am. 75, 1765–1782.
Vidale, J.E., Ellsworth, W.L., Cole, A., Marone, C., 1994. Rupture variation with recurrence interval in eighteen cycles of a small earthquake. Nature 368, 624–626.
Wald, D.J., Heaton, T.H., 1994. Spatial and temporal distribution of slip for the 1992 Landers, California, earthquake. Bull. Seismol. Soc. Am. 84, 668–691.
Wesnousky, S.G., 2006. Predicting the endpoints of earthquake ruptures. Nature 444 (16), 358–360.
Wesnousky, S.G., 2008. Displacement and geometrical characteristics of earthquake surface ruptures: issues and implications for seismic-hazard analysis and the process of earthquake rupture. Bull. Seismol. Soc. Am. 98 (4), 1609–1632.
Wu, J., Hole, J.A., Snoke, J.A., 2010. Fault-zone structure at depth from differential dispersion of seismic guided waves: evidence for a deep waveguide on the San Andreas fault. Geophys. J. Int. 182, 343–354. http://dx.doi.org/10.1111/j.1365-246X.2010.04612.x.